

# ON THE DESIGN OF A FLEXIBLE WAVEFORM AND LOW ICI SYMBOL BOUNDARY ALIGNMENT

A THESIS SUBMITTED TO  
THE GRADUATE SCHOOL OF  
ENGINEERING AND NATURAL SCIENCES  
OF ISTANBUL MEDIPOL UNIVERSITY

IN PARTIAL FULFILLMENT OF THE REQUIREMENTS FOR

THE DEGREE OF

MASTER OF SCIENCE

IN

ELECTRICAL, ELECTRONICS ENGINEERING AND CYBER SYSTEMS

By

Mahyar Nemati

December, 2017

On the Design of a Flexible Waveform and Low ICI Symbol Boundary  
Alignment

By Mahyar Nemati

December, 2017

We certify that we have read this thesis and that in our opinion it is fully adequate,  
in scope and in quality, as a thesis for the degree of Master of Science.



---

Prof. Dr. Hüseyin Arslan(Advisor)



---

Assoc. Prof. Dr. Ertuğrul Başar



---

Assist. Prof. Dr. Tunçer Baykaş

Approved by the Graduate School of Engineering and Natural Sciences:



---

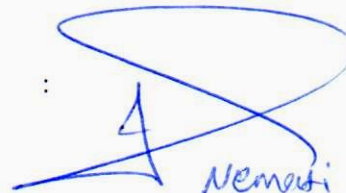
Prof. Dr. Talip Alp

Director of the Graduate School of Engineering and Natural Sciences

I hereby declare that all information in this document has been obtained and presented in accordance with academic rules and ethical conduct. I also declare that, as required by these rules and conduct, I have fully cited and referenced all material and results that are not original to this work.

Name, Last Name: MAHYAR NEMATI

Signature :



# ABSTRACT

## ON THE DESIGN OF A FLEXIBLE WAVEFORM AND LOW ICI SYMBOL BOUNDARY ALIGNMENT

Mahyar Nemati

M.S. in Electrical, Electronics Engineering and Cyber Systems

Advisor: Prof. Dr. Hüseyin Arslan

December, 2017

Cellular systems of fifth generation (5G) radio access technology is expected to support a wide variety of service requirements in different applications. High reliability, flexibility, spectral efficiency, and low power consumption are some of the service requirements. In order to support these requirements, symbol boundary alignment design and the waveform selection play important roles. The current symbol boundary alignment, along with orthogonal frequency division multiplexing (OFDM) waveform, has some disadvantages, such as non-flexible guard interval (e.g., hard coded cyclic prefix (CP)), and severe intercarrier interference (ICI) in high speed communications like in unmanned aerial vehicles (UAV).

In the literature, multiple different waveforms are proposed to be used instead of the OFDM in 5G. Although they try to prevent from the drawbacks of OFDM, they create other problems such as high complexity. Among the available waveform candidates, zero tail (ZT) DFT-spread (s) OFDM has flexible GI and low power consumption along with a low complex transceiver. However, unlike its name, ZT DFT-s OFDM contains non-zero samples at its tail causing intersymbol interference (ISI) in multipath channels. Additionally, ZT DFT-s OFDM does not solve the ICI problem of high speed communications. Regarding to these issues, this thesis presents two separate solutions as follows.

First, an improved version of ZT DFT-s OFDM, called DFT-s zero word (ZW) OFDM, is proposed to reduce the ISI power. In DFT-s ZW OFDM, we utilize redundant subcarriers concept, like in unique word (UW) OFDM, to nullify the tail of ZT DFT-s OFDM. The achieved waveform benefits from high mitigation in the ISI power compared to ZT DFT-s OFDM. Although DFT-s ZW OFDM has a superior performance in multipath channels, it consumes slightly more power than ZT DFT-s OFDM. Therefore, a hybrid waveform, constructed by ZT DFT-s OFDM and DFT-s ZW OFDM, is designed which provides a high flexibility in order to control the symbol power and bit error rate (BER) performance of the

system. The hybrid waveform utilizes the similarity between the transceivers of these two waveforms to deploy them in one resource block (RB) for a user. Thus, it can control the symbol power, reliability, and even peak to average power ratio (PAPR) of the system by tuning the dedicated subcarriers to each waveform with respect to the channel characteristics.

The second part of this thesis focuses on ICI reduction in current LTE numerologies and presents a novel symbol boundary alignment called “Low ICI Symbol boundary alignment numerology (LICIS)”. LICIS utilizes large subcarrier-spacing to reduce the ICI power (e.g. around 5 dB ICI power reduction with subcarrier-spacing of 30 kHz in high speed UAV communications). Moreover, LICIS is based on the same reference clock as LTE which guarantees its compatibility with the current LTE numerology. Additionally, this approach places only one guard-interval (GI) at the end of a sequence of OFDM symbols and creates a sub-slot. It leads to less overhead and preserves the spectral efficiency. Furthermore, a pre-FFT multipath channel equalizer is considered for preventing the intersymbol interference (ISI) between the OFDM symbols occurring within the sub-slot. However, only one additional FFT and IFFT operations are required for the equalizer which creates an acceptable complexity increment compared to the complexity of other available solutions. Numerical and analytical evaluations show the superior performance of the proposed technique in terms of reliability and spectral efficiency.

*Keywords:* Flexibility, Guard interval (GI), Intercarrier interference (ICI), Intersymbol interference, Numerology, Spectral efficiency, Symbol boundary alignment, Waveform.

## ÖZET

# ESNEK WAVEFORM VE DÜŞÜK GİRİŞİMLİ SEMBOL SINIRI HIZALAMA TASARIMI HAKKINDA

Mahyar Nemati

Elektrik-Elektronik Mühendisliği ve Siber Sistemler, Yüksek Lisans

Tez Danışmanı: Prof. Dr. Hüseyin Arslan

Aralık, 2017

Beşinci nesil (5G) radyo erişim teknolojisinin hücreli sistemleri çok çeşitli hizmet gereksinimlerini farklı uygulamaları desteklemesi bekleniyor. Yüksek güvenilirlik, esneklik, spektral verimlilik, ve düşük güç tüketimi bazı hizmet gereksinimleridir. Bu gereksinimleri desteklemek için sembol sınır hizalama tasarımı ve dalga formu seçimi önemli rol oynamaktadır. Bu konularda bu tez şu şekilde iki ayrı çözüm sunmaktadır:

Birincisi, ZT DFT-s OFDM'nin geliştirilmiş bir versiyonu olan DFT-s ZW OFDM, ISI gücünü azaltmak için önerildi. DFT-s ZW OFDM'de, ZT DFT-s OFDM kuyruğunu geçersiz kılıyoruz.

Bu tezin ikinci bölümünde, mevcut LTE numerolojilerinde ICI azalması üzerinde duruluyor ve "Düşük ICI Sembol Sınır Hizalama (LICIS)" numerolojisi olarak adlandırılan yeni bir sembol sınır hizalanması sunuluyor.

*Anahtar sözcükler:* Esneklik, Koruma aralığı, Araçlar arası girişim, Semboller arası girişim, Numeroloji, Spektral verimlilik, Sembol sınır hizalaması, Dalga biçimi.

## Acknowledgement

I would like to express my deepest gratitude to my advisor Prof. Hüseyin Arslan for his continuous guidance and for introducing me to the exciting and promising topic of physical layer architecture. Indeed, with his encouragement, expertise and advice, the goals of the thesis were successfully achieved.

In addition, I want to express my heartfelt appreciation to my family and friends for their continuous encouragement and their moral support.

# Contents

<b>1</b>	<b>Introduction</b>	<b>1</b>
1.1	Flexibility in waveform design . . . . .	2
1.2	ICI problem in high speed communications . . . . .	3
1.3	Thesis outline . . . . .	4
<b>2</b>	<b>Discrete Fourier Transform Spread Zero Word OFDM</b>	<b>7</b>
2.1	Transmitter side . . . . .	7
2.1.1	Receiver side . . . . .	13
2.2	Performance Evaluation . . . . .	15
2.3	Conclusions . . . . .	19
<b>3</b>	<b>A Flexible Hybrid Waveform</b>	<b>20</b>
3.1	System Description and Properties . . . . .	20
3.1.1	Zero Tail DFT Spread OFDM . . . . .	20
3.1.2	DFT Spread Zero Word OFDM . . . . .	22



3.1.3	Hybrid Model . . . . .	23
3.2	Implementation and Complexity . . . . .	24
3.3	Numerical Results . . . . .	28
3.3.1	Power Evaluation . . . . .	28
3.3.2	Bit Error Rate . . . . .	29
3.3.3	Out of Band Emission . . . . .	30
3.3.4	Peak to Average Power Ratio . . . . .	30
3.4	Conclusions and Future Research . . . . .	31
<b>4</b>	<b>Low ICI Symbol Boundary Alignment</b>	<b>32</b>
4.1	Conventional Symbol Boundary Alignment Numerology . . . . .	32
4.2	Low ICI Symbol Boundary Alignment Numerology (LICIS) . . . . .	34
4.2.1	Guard Interval Selection . . . . .	35
4.2.2	Complexity Analysis . . . . .	43
4.3	Spectral Efficiency Analysis . . . . .	44
4.4	ICI Distortion Expression . . . . .	46
4.5	Numerical Results . . . . .	47
4.5.1	Symbol Error Rate Performance . . . . .	48
4.5.2	Spectral Efficiency Evaluation . . . . .	48
4.5.3	Average Error Vector Magnitude Distribution . . . . .	50

4.5.4 ICI power versus normalized Doppler shift . . . . . 51

4.6 Conclusions . . . . . 52

**5 Concluding Remarks 53**

5.1 Summary . . . . . 53

**Bibliography 55**



# List of Figures

2.1	Transmitter side of DFT-s ZW OFDM. . . . .	8
2.2	Receiver side of DFT-s ZW OFDM. . . . .	8
2.3	Transmitted signals in the time domain. . . . .	10
2.4	Flexibility comparison in terms of keeping orthogonality when having different lengths for guard interval. . . . .	11
2.5	PAPR comparison. [left:] with considering tails, [right:] without considering tails. . . . .	15
2.6	Power spectral density comparison. . . . .	16
2.7	BER comparison for the AWGN channel. . . . .	17
2.8	BER comparison in Rayleigh fading channel. . . . .	18
3.1	Comparison of symbol power and tail power in ZT DFT-s OFDM, DFT-s ZW-OFDM and Hybrid model. . . . .	21
3.2	Co-existence of two waveforms as two Sub-RBs with equal symbol periods and guard intervals. . . . .	22
3.3	Co-locating ZW and ZT subcarriers without a guard between them.	23

3.4	Size of sub-RBs is controlled by resource allocation decision (RAD) block checking the user requirements. . . . .	24
3.5	Block diagram of the proposed hybrid waveform. . . . .	25
3.6	Comparison of power in the tail of hybrid model and conventional ZT-DFT-s-OFDM. Tail power increases as $N_{zt}$ increases. . . . .	28
3.7	Symbol power of hybrid model decreases as $N_{zt}$ increases. . . . .	29
3.8	BER performance of the hybrid waveform in Rayleigh fading channel with uniform PDP distribution, $\tau = 21$ . . . . .	30
3.9	Power spectral density comparison. . . . .	31
4.1	Conventional LTE numerology as a reference numerology for LICIS. . . . .	33
4.2	Spectral inefficient numerology with large subcarrier-spacing and short symbol duration ( $\Delta f_q \sim \omega_q \rightarrow \frac{T_\ell}{q}$ ). . . . .	33
4.3	LICIS structure. $M$ OFDM symbols with $\Delta f_\rho$ are inserted back to back and Only one GI exists at the end of them ( $M = \rho = 4$ ). . . . .	34
4.4	Illustration of sub-slot, slot and TTI in LICIS. LICIS is based on the same reference clock as LTE. . . . .	35
4.5	Conventional symbol boundary alignment with $\Delta f_s$ does not have ISI. . . . .	36
4.6	Conventional symbol boundary alignment with $\Delta f_q$ does not have ISI, ( $q = 2$ ). . . . .	36
4.7	LICIS has ISI inside one sub-slot ( $M = \rho = 2$ ). . . . .	36
4.8	The effect of Doppler shift over OFDM sub-carriers. . . . .	40

4.9	Transmitter and receiver block diagram of the LICIS. . . . .	42
4.10	PDP of the multipath Rayleigh fading channel without Doppler effect ( $\tau_{\max} = 16t_s$ ). . . . .	48
4.11	4-QAM SER performance comparison where $V_\mu = 200$ km/h and $f_{d_{\max}} = 0.07\Delta f_s$ ( $M = \rho$ ). . . . .	49
4.12	4-QAM SER performance comparison where $V_\mu = 500$ km/h and $f_{d_{\max}} = 0.19\Delta f_s$ ( $M = \rho$ ). . . . .	49
4.13	4-QAM spectral efficiency performance comparison where $V_\mu = 500$ km/h and $f_{d_{\max}} = 0.19\Delta f_s$ ( $M = \rho$ ). . . . .	50
4.14	64-QAM and 4-QAM spectral efficiency performance comparison where $V_\mu = 500$ km/h and $f_{d_{\max}} = 0.19\Delta f_s$ ( $M = \rho$ ). . . . .	50
4.15	4-QAM EVM distribution comparison where $V_\mu = 500$ km/h and $f_{d_{\max}} = 0.19\Delta f_s$ . . . . .	51
4.16	Simulation and theoretical results for the ICI power on a subcarrier versus normalized frequency Doppler shift. . . . .	51

# List of Tables

2.1	Comparison between various waveforms . . . . .	19
4.1	Complexity comparison of transceivers in conventional LTE numerology and LICIS ( $M = \rho \Rightarrow T_\ell = \mathfrak{L} = \rho T_\rho$ ). . . . .	44

# Chapter 1

## Introduction

Fifth Generation (5G) of mobile communications is coming and the demand for a better mobile communication is increasing quickly. High capacity and flexibility beside low latency and power consumption are the most important performance requirements to be met by 5G [1]. In order to respond and satisfy the imposed requirements, waveform design plays a key role. The fourth generation waveform, Orthogonal Frequency Division Multiplexing (OFDM), while providing a lot of advantages, leads to large out of band (OOB) emission and peak to average power ratio (PAPR), and requires cyclic prefix (CP). Additionally, it strongly suffers from intercarrier interference (ICI) in high speed communications like in unmanned aerial vehicles (UAV) where the mobility causes Doppler effect which leads to loss of orthogonality in OFDM [2]. The loss of orthogonality gets even worse in high speed UAV communications, where the speed can go up to hundreds km/h [3]. Consequently, a severe ICI is created which degrades the reliability of the communications severely. These disadvantages make the OFDM inefficient for most of the 5G applications.

## 1.1 Flexibility in waveform design

Different use cases in 5G, with different requirements are defined, with flexibility being one of the most important design principles. This flexibility can be in the guard interval length, subcarrier spacing, etc. Adding a CP as a guard interval is one of the most famous methods to avoid intersymbol interference (ISI). However, having a CP in the whole range of use cases and channels leads to some inefficiencies in terms of spectrum and power. Additionally, different CP lengths result in different frame durations. In long term evolution (LTE), there are different hard coded CP durations, short and long. However, due to loss of orthogonality between these two frame durations, the system experiences interference. Removing the interference requires a computational complexity and hence inefficient receiver [4]. Among the potential 5G waveforms such as, Universal Filtered Multi-Carrier (UFMC), Filter-Bank Multi-Carrier (FBMC), Filtered (F)-OFDM, Generalized Frequency Division Multiplexing (GFDM), Zero Tail (ZT) DFT-spread (s)-OFDM, Unique Word (UW) OFDM and DFT-s-OFDM [4, 5, 6, 7, 8, 9, 10, 11, 12], only ZT DFT-s-OFDM and UW-OFDM provide more flexibility in terms of tail (guard interval) lengths. In both techniques, transmitted signal contains low power samples at the tails. These samples are part of the IFFT output, and as such, are different from CP-OFDM, where the CP is appended after IFFT output. However, these two flexible waveforms have some disadvantages. On the one hand, UW-OFDM suffers from high PAPR due to the high power of redundant subcarriers. On the other hand, the tail samples in ZT DFT-s-OFDM are not exactly zero, have a lower power compared to the non-tail symbol part, which remains non-negligible and results in ISI. To suppress this tail in ZT DFT-s-OFDM, a recent study in [13] has proposed the use of redundant symbols in the time domain. This solution dedicates a number of DFT inputs to redundant symbols with a certain amount of power that introduces ISI intrinsically in low SNRs. It also requires to optimize the value of the redundant symbols for each transmitted symbol which increases complexity and latency of the system.

At the end, we can say that none of the presented waveforms can not be



used as a unique waveform design for the 5G. In other words, 5G need to obtain a hybrid version of waveforms to acheive their advantages while avoiding their disadvantages.

## 1.2 ICI problem in high speed communications

ICI is the type of frequency distortion due to the interference of other subcarriers with the intended subcarrier [14]. Doppler effect (including Doppler spread and Doppler shift) and carrier frequency offset (CFO) are the main reasons of frequency distortion in frequency dispersive channels. ICI has been always a critical issue in multicarrier-based communications. In the literature, a significant effort has been done in order to overcome it. However, the available solutions have some drawbacks, such as high complexity, low spectral efficiency, and incompatibility with the current radio access technologies.

For instance, in recent surveys and researches, (e.g., [15, 16, 17, 18, 19] and their references), authors evaluate different types of ICI reduction techniques. However, they suffer from a multi step equalization which results in high complexity. The number of steps is even increased in high speed UAV communications.

Recently, a new technique based on fractional Fourier transform (FrFT)-OFDM is proposed in [20], where authors found the near optimum angle of transform in FrFT-OFDM to minimize the bound of ICI power. Besides the complexity issues, angle of transform varies with Doppler severity and the angle approaches zero by increasing Doppler shift which leads to a single carrier transmission.

Another technique, in [21], utilizes small subblock frequency domain equalizations (FDE) by exploiting a pseudo cyclic prefix (CP) technique instead of the real guard interval (GI) in each subblock. However, it requires more FDE steps in high speed communications. Additionally, the reliability of this method is not

guaranteed properly due to subtraction of an estimated part from the received signal.

In [22, 23, 24], authors propose to use filtered subcarrier blocks. They consider each block of subcarriers as a resource block (RB) which can be filtered for transmission. This approach restricts the ICI inside only one RB with the expense of filtering issues. However, ICI problem still exists severely inside that RB.

Utilizing large subcarrier-spacing for high speed users is another solution which is considered in the literature (e.g., [25, 26, 27]). However, by increasing the subcarrier-spacing, the symbol duration in the time domain is decreased. Therefore, the number of symbols in one transmission time interval is increased and a greater number of GI is required to prevent intersymbol interference (ISI). Thus, it decreases the spectral efficiency. In addition, using large subcarrier-spacing for high speed users and small subcarrier-spacing for low speed users leads to different symbol durations. It changes the synchronous transmission to an asynchronous transmission [27]. Consequently, handling the asynchronous communications has its own complex solutions (e.g., using filters to suppress the out of band emission of subcarriers to avoid interference between different users).

### 1.3 Thesis outline

The goal of this thesis is to propose a flexible waveform design to have a unique waveform which can be adapted with the service requirements. The other goal is to propose a simple solution for ICI power reduction in OFDM which can be used in future applications.

In chapter 2, we propose a new and efficient waveform that has a good PAPR, OOB emission, power efficiency and bit error rate (BER) performance. In the proposed model, called **DFT Spread Zero Word (ZW) OFDM**, we nullify the tail of ZT DFT-s-OFDM, using the unique word technique. The resulting model has the advantages of both ZT DFT-s-OFDM and UW-OFDM waveforms, while

avoiding their disadvantages. The advantages of our proposed model compared to CP-OFDM, ZT DFT-s-OFDM and UW-OFDM are:

- Zero tail power compared to the ZT DFT-s-OFDM leading to a satisfactory solution for the ISI issue.
- Lower PAPR and better power efficiency, compared to UW-OFDM and CP-OFDM, due to the single carrier nature of DFT-s-ZW-OFDM.
- Flexible and controllable low power tail compared to fixed CP length, in CP-OFDM.

Chapter 3 studies ZT-DFT-s-OFDM and the improved UW-OFDM waveform called DFT-s-ZW-OFDM in order to obtain the hybrid waveform in one UL resource block (RB) in the cellular networks.

Chapter 4 presents a novel approach, called **Low ICI Symbol boundary alignment numerology (LICIS)**, which reduces the ICI while preserving the spectral efficiency. Contrary to the presented techniques, LICIS does not need a high complex equalization technique or different waveform structure. It only manipulates the conventional symbol boundary alignment numerology to obtain a new symbol boundary alignment which achieves a superior performances. LICIS utilizes large subcarrier-spacing to reduce the ICI power. In addition, this approach places only one GI at the end of a sequence of OFDM symbols and creates a sub-slot. Therefore, there is no GI between the OFDM symbols inside the sub-slot. It leads to have less overhead and consequently preserves the spectral efficiency. Furthermore, a pre-FFT multipath channel equalizer is used to prevent the ISI inside a sub-slot as well. Only one additional FFT and IFFT operations are required for the equalizer which creates an acceptable complexity increment compared to the complexity of other presented solutions. Also, LICIS is based on the same reference clock as LTE which assures its compatibility with the current LTE numerology.

Finally, chapter 5 concludes this thesis, where we highlight our main findings, summarize the main results.

**Notations:**  $(\cdot)$  is used to denote the frequency domain transform of a vector

or a matrix.  $\mathbf{I}$  and  $\mathbf{O}$  denote the identity and zero matrices, respectively.  $(\cdot)^T$  and  $(\cdot)^H$  indicate Transposition and Hermitian operations, respectively.  $\mathbf{E}[\cdot]$  and  $tr(\cdot)$  denote expected value and trace of a matrix, respectively.



## Chapter 2

# Discrete Fourier Transform Spread Zero Word OFDM

The block diagram of the proposed scheme is shown in Figs. 2.1 and 2.2 . The procedures in the transmitter and receiver sides are divided into four steps, to be explained.

### 2.1 Transmitter side

In step one at the transmitter,  $N$  data symbols go through an  $N$ -point DFT block in order to be spread in the frequency domain. If  $\mathbf{d}$  and  $\tilde{\mathbf{d}}$  denote the data vectors in the time and frequency domain resultant, respectively, then we have

$$\tilde{\mathbf{d}}_{(N \times 1)} = \mathbf{D}_{(N \times N)} \times \mathbf{d}_{(N \times 1)}, \quad (2.1)$$

where  $\mathbf{D}$  is the DFT matrix.

In step two, the zero word is generated by adding a set of redundant subcarriers. Values of the redundant subcarriers depend on data and need to be defined

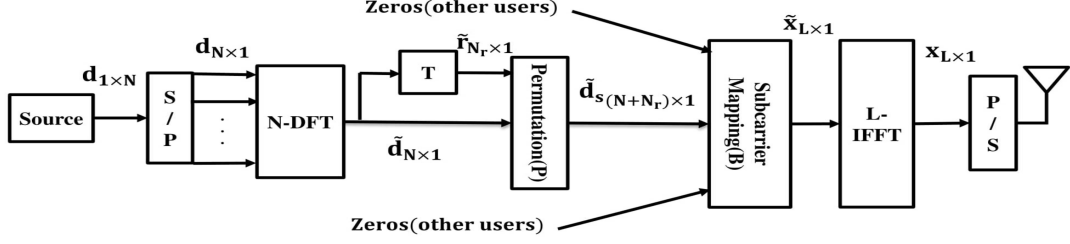


Fig. 2.1: Transmitter side of DFT-s ZW OFDM.

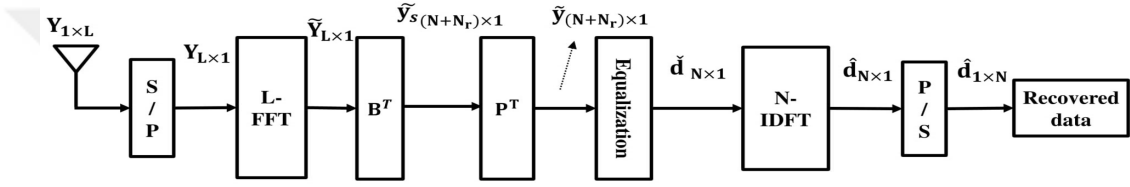


Fig. 2.2: Receiver side of DFT-s ZW OFDM.

as

$$\begin{aligned}
 \tilde{\mathbf{r}}_{(N_r \times 1)} &= \mathbf{T}_{(N_r \times N)} \times \tilde{\mathbf{d}}_{(N \times 1)} \\
 &= \mathbf{T}_{(N_r \times N)} \times \mathbf{D}_{(N \times N)} \times \mathbf{d}_{(N \times 1)}.
 \end{aligned} \tag{2.2}$$

The corresponding vector ( $\tilde{\mathbf{r}}_{(N_r \times 1)}$ ), comprising  $N_r$  components, is therefore expressed as redundant subcarrier vector. In (2.2),  $\mathbf{T}$  is a transformation matrix establishing a relationship between the data and redundant subcarriers, to be optimized next. It is worth mentioning that with spreading data on all subcarriers using matrix  $\mathbf{D}_{(N \times N)}$ , we achieve lower PAPR than conventional UW-OFDM proposed in [10] due to single carrier nature of DFT-s-ZW-OFDM.

In step three, redundant subcarriers are appended to data subcarriers, followed by a subcarrier permutation and mapping to the IFFT bins. The redundant subcarriers are permuted between data subcarriers by permutation matrix  $\mathbf{P} \in \{0, 1\}^{(N+N_r) \times (N+N_r)}$  and the mapping is done by inserting unused zero subcarriers in IFFT bins for each user by mapping matrix  $\mathbf{B} \in \{0, 1\}^{(L) \times (N+N_r)}$  as shown in Fig. 2.1. The mapping could be either localized or distributed. Localized mapping provides multi-user scheduling gain in the frequency domain while distributed mapping results in lower PAPR. First, permutation operation is done

as

$$\tilde{\mathbf{d}}_{\mathbf{s}(N+N_r) \times 1} = \mathbf{P}_{(N+N_r) \times (N+N_r)} \begin{bmatrix} \mathbf{D}_N \mathbf{d} \\ \tilde{\mathbf{r}} \end{bmatrix}_{(N+N_r) \times 1}, \quad (2.3)$$

then, mapping step with respect to the localized or distributed mapping is done as

$$\tilde{\mathbf{x}}_{L \times 1} = \mathbf{B}_{L \times (N+N_r)} \times \tilde{\mathbf{d}}_{\mathbf{s}(N+N_r) \times 1}, \quad (2.4)$$

where the IFFT input is denoted by  $\tilde{\mathbf{x}}$ .

In step four, the resulting subcarriers, totalizing  $N + N_r$  plus zero subcarriers, are passed through an  $L$ -point IFFT, where  $L > N + N_r$ , to end up with the signal to be transmitted.  $L$ -point IFFT matrix and transmitted signal are denoted by  $\mathbf{F}_L^{-1}$  and  $\mathbf{x}$ , respectively. Using these notations and (2.1), (2.2), (2.3), (2.4), the transmitted signal can be expressed as

$$\mathbf{x} = \mathbf{F}_L^{-1} \tilde{\mathbf{x}}_{L \times 1} \quad (2.5)$$

$$= \overbrace{\mathbf{F}_L^{-1} \mathbf{B} \mathbf{P}}^{\mathbf{M}} \begin{bmatrix} \mathbf{I} \\ \mathbf{T} \end{bmatrix} \mathbf{D}_N \mathbf{d} \quad (2.6)$$

where  $\mathbf{M}$  can be divided into four submatrices

$$\mathbf{M} = \begin{bmatrix} \mathbf{M}_{11} & \mathbf{M}_{12} \\ \mathbf{M}_{21} & \mathbf{M}_{22} \end{bmatrix}. \quad (2.7)$$

To determine the transformation matrix  $\mathbf{T}$  which provides zero tailing, we split the transmitted signal into two parts, namely  $\mathbf{x}_{\text{non\_tail}}$  and  $\mathbf{x}_{\text{tail}}$  represented as  $\begin{bmatrix} \mathbf{x}_{\text{non\_tail}} \\ \mathbf{x}_{\text{tail}} \end{bmatrix}$ .  $\mathbf{x}_{\text{tail}}$  has  $N_{zw}$  samples where  $N_r \geq N_{zw}$  [10]. The optimum case for having least redundancy is  $N_r = N_{zw}$ . In this case,  $\mathbf{M}_{11}$  and  $\mathbf{M}_{22}$  are square, non-singular and invertible matrices with respect to  $\mathbf{P}$ . In order to make  $\mathbf{x}_{\text{tail}}$

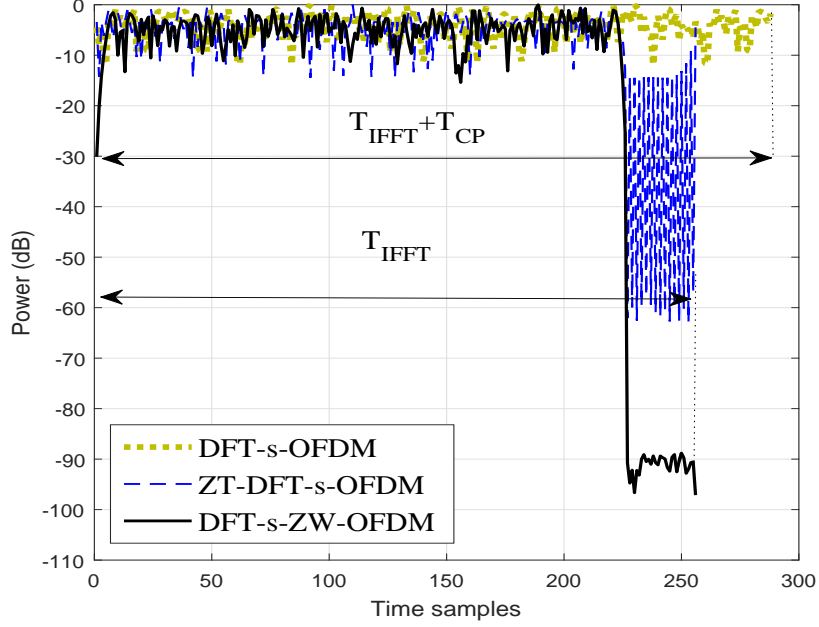


Fig. 2.3: Transmitted signals in the time domain.

zero, it is required to have

$$\begin{bmatrix} \mathbf{x}_{\text{non\_tail}} \\ 0 \end{bmatrix} = \begin{bmatrix} \mathbf{M}_{11(N \times N)} & \mathbf{M}_{12(N \times N_r)} \\ \mathbf{M}_{21(N_r \times N)} & \mathbf{M}_{22(N_r \times N_r)} \end{bmatrix} \begin{bmatrix} \mathbf{D}_N \mathbf{d} \\ \tilde{\mathbf{r}} \end{bmatrix}, \quad (2.8)$$

which means that

$$\tilde{\mathbf{r}} = -\mathbf{M}_{22}^{-1} \mathbf{M}_{21} \overbrace{\mathbf{D}_N \mathbf{d}}^{\tilde{\mathbf{a}}}. \quad (2.9)$$

The required transformation is therefore given by (2.10) as

$$\mathbf{T} = -\mathbf{M}_{22}^{-1} \mathbf{M}_{21}. \quad (2.10)$$

It is worth mentioning that in the proposed waveform, zeros are not appended to the end of the signal (zero padding [28]), but they are created using the redundant subcarriers, within IFFT duration ( $T_{IFFT}$ ), (Figs. 2.3 and 2.4).

**Complexity:** To examine the complexity, one of the important issues in adding redundant subcarriers is the energy to be allocated at the transmitter



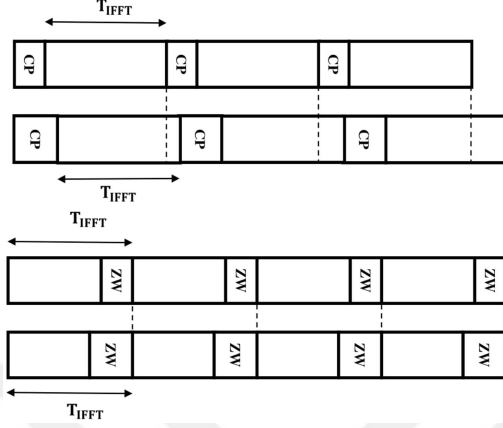


Fig. 2.4: Flexibility comparison in terms of keeping orthogonality when having different lengths for guard interval.

for each one of them, incurs in energy inefficiency. The energy of redundant subcarriers can be high and the performance of the proposed model can be compromised by it. Energy of the transmitted signal  $E_x$  can be computed as

$$E_x = \mathbf{E}[\mathbf{x}^H \mathbf{x}], \quad (2.11)$$

by substituting (2.5) in (2.11), followings are given

$$\begin{aligned}
E_x &= \mathbf{E}[(\mathbf{F}_L^{-1} \tilde{\mathbf{x}})^H \mathbf{F}_L^{-1} \tilde{\mathbf{x}}] = \frac{1}{L} \mathbf{E}[\tilde{\mathbf{x}}^H \mathbf{I}_L \tilde{\mathbf{x}}] \\
&= \frac{1}{L} \mathbf{E} \left[ [(\mathbf{D}_N \mathbf{d})^H \tilde{\mathbf{r}}^H] \mathbf{P}^T \mathbf{B}^T \mathbf{B} \mathbf{P} \begin{bmatrix} \mathbf{D}_N \mathbf{d} \\ \tilde{\mathbf{r}} \end{bmatrix} \right] \\
&= \frac{1}{L} \mathbf{E} \left[ [(\mathbf{D}_N \mathbf{d})^H \tilde{\mathbf{r}}^H] \begin{bmatrix} \mathbf{D}_N \mathbf{d} \\ \tilde{\mathbf{r}} \end{bmatrix} \right] \\
&= \frac{1}{L} (\mathbf{E}[(\mathbf{D}_N \mathbf{d})^H \mathbf{D}_N \mathbf{d}] + \mathbf{E}[\tilde{\mathbf{r}}^H \tilde{\mathbf{r}}]) \\
&= \frac{1}{L} (N \mathbf{E}[\mathbf{d}^H \mathbf{I}_N \mathbf{d}] + \mathbf{E}[\tilde{\mathbf{r}}^H \tilde{\mathbf{r}}]) \\
&= \underbrace{\frac{N}{L} \mathbf{E}[\mathbf{d}^H \mathbf{d}]}_{E_d} + \underbrace{\frac{1}{L} \mathbf{E}[\tilde{\mathbf{r}}^H \tilde{\mathbf{r}}]}_{E_r}, \quad (2.12)
\end{aligned}$$

where  $E_d$  and  $E_r$  are energies of data and redundant subcarriers, respectively. By assuming that the data symbols are uncorrelated with zero mean and variance

$\sigma_d^2$ , we have

$$E_d = \frac{N}{L}(N\sigma_d^2) = \frac{N^2}{L}\sigma_d^2. \quad (2.13)$$

$E_r$  can be written as

$$\begin{aligned} E_r &= \frac{1}{L}\mathbf{E}[\tilde{\mathbf{r}}^H\tilde{\mathbf{r}}] = \frac{1}{L}\mathbf{E}[tr(\tilde{\mathbf{r}}\tilde{\mathbf{r}}^H)] = \frac{1}{L}tr(\mathbf{E}[\tilde{\mathbf{r}}\tilde{\mathbf{r}}^H]) \\ &= \frac{1}{L}tr(\mathbf{E}[\mathbf{T}\tilde{\mathbf{d}}\tilde{\mathbf{d}}^H\mathbf{T}^H]) = \frac{1}{L}tr(\mathbf{T}\mathbf{E}[\tilde{\mathbf{d}}\tilde{\mathbf{d}}^H]\mathbf{T}^H) \\ &= \frac{1}{L}(tr(\mathbf{T}\mathbf{D}_N\underbrace{\mathbf{E}[\mathbf{d}\mathbf{d}^H]}_{\sigma_d^2}\mathbf{D}_N^H\mathbf{T}^H)) \\ &= \frac{N\sigma_d^2}{L}(tr(\mathbf{T}\mathbf{T}^H)). \end{aligned} \quad (2.14)$$

Substituting (2.13) and (2.14) in (2.12)

$$E_x = \frac{N^2\sigma_d^2}{L} + \frac{N\sigma_d^2}{L}(tr(\mathbf{T}\mathbf{T}^H)). \quad (2.15)$$

To minimize  $E_x$ ,  $tr(\mathbf{T}\mathbf{T}^H)$  should be minimized. Based on  $\mathbf{T}$  in (2.10) and  $\mathbf{M}$  in (2.6),  $tr(\mathbf{T}\mathbf{T}^H)$  does not depend on data, however, highly depends on the permutation matrix ( $\mathbf{P}$ ), thus for a fixed  $N$ ,  $N_r$ ,  $L$  and mapping matrix,  $\mathbf{P}$  needs to be found **once** in the system that increases the complexity **slightly** (Table 2.1). The number of possible  $\mathbf{P}$ s is  $\binom{N+N_r}{N_r}$ . Combinatorial search algorithms are typically concerned non-deterministic polynomial-time hard (NP-hard) problems. There is a heuristic algorithm for finding a permutation which corresponds to a local optimum in [10] which gives a suboptimum  $\mathbf{P}$ . We utilize the algorithm to get suboptimum low power redundant subcarrier positions.

Note that matrix  $\mathbf{B}$  only maps the data to the intended subcarriers and does not increase the complexity of the system. Next, we follow the process at the receiver side, the block diagram of which is shown in Fig. 2.2.

### 2.1.1 Receiver side

It is worth mentioning that both receiver and transmitter have got the knowledge of  $\mathbf{P}$  and  $\mathbf{B}$  matrices. At the receiver side, the received signal, after passing through the channel shorter than zero word, can be expressed by  $\mathbf{Y}$  as

$$\mathbf{Y} = \mathbf{H}_c \mathbf{x} + \mathbf{n}, \quad (2.16)$$

where  $\mathbf{H}_c$  is the cyclic-convolution matrix corresponding to the channel. It should be noted that due to the repetition of zero word, cyclic convolution can be used instead of linear convolution. A discrete time zero mean additive white Gaussian noise (AWGN) with the variance of  $\sigma_n$  is denoted by  $\mathbf{n}$ . Substituting  $\mathbf{x}$  from (2.6) into (2.16),

$$\mathbf{Y} = \mathbf{H}_c \mathbf{F}_L^{-1} \mathbf{B} \mathbf{P} \begin{bmatrix} \mathbf{I} \\ \mathbf{T} \end{bmatrix} \mathbf{D}_N \mathbf{d} + \mathbf{n}. \quad (2.17)$$

As shown in Fig. 2.2, the receiver operations is almost inverse of the transmitter operations and the received signal goes through the following steps:

In step one, the received signal is passed through an  $L$ -point FFT as shown in Fig. 2.2.

$$\tilde{\mathbf{Y}}_{L \times 1} = \mathbf{F}_L \mathbf{Y}. \quad (2.18)$$

In step two,  $\mathbf{B}^T$  and  $\mathbf{P}^T$  matrices are used to do inverse operations of mapping and permutation, respectively.  $\mathbf{B}^T$  removes unused zero subcarriers as follows

$$\tilde{\mathbf{y}}_{s(N+N_r) \times 1} = \mathbf{B}^T_{(N+N_r) \times L} \tilde{\mathbf{Y}}_{L \times 1}, \quad (2.19)$$

where  $\tilde{\mathbf{y}}_s$  is the output of inverse operation of mapping. This operation transforms the output from  $\mathbb{C}^{L \times 1}$  to  $\mathbb{C}^{(N+N_r) \times 1}$ . Mathematical representation of inverse operation of permutation using  $\mathbf{P}^T$  and (2.18), (2.19) can be expressed as:

$$\tilde{\mathbf{y}}_{(N+N_r) \times 1} = \mathbf{P}^T_{(N+N_r) \times (N+N_r)} \tilde{\mathbf{y}}_{s(N+N_r) \times 1} \quad (2.20)$$

$$= \mathbf{P}^T \mathbf{B}^T \mathbf{F}_L \mathbf{Y}. \quad (2.21)$$

$\mathbf{P}^T$  sorts the subcarriers in order to have data subcarriers at the first

$N$  positions and the redundant subcarriers at the end, represented as  $\begin{bmatrix} \text{data subcarriers}_{(N \times 1)} \\ \text{redundant subcarriers}_{(N_r \times 1)} \end{bmatrix}$ . Substituting (2.17) into (2.21) results in

$$\begin{aligned} \tilde{\mathbf{y}} &= \underbrace{\mathbf{P}^T \mathbf{B}^T \mathbf{F}_L \mathbf{H}_c \mathbf{F}_L^{-1} \mathbf{B} \mathbf{P}}_{\mathbf{H}} \underbrace{\begin{bmatrix} \mathbf{I} \\ \mathbf{T} \end{bmatrix}}_{\mathbf{G}} \underbrace{\mathbf{D}_N \mathbf{d}}_{\check{\mathbf{d}}} + \underbrace{\mathbf{P}^T \mathbf{B}^T \mathbf{F}_L \mathbf{n}}_{\mathbf{n}'} \\ &= \mathbf{H} \mathbf{G} \check{\mathbf{d}} + \mathbf{n}'. \end{aligned} \quad (2.22)$$

For simplicity of notation,  $\mathbf{H}$  represents the above shown part of the  $\tilde{\mathbf{y}}$  and  $\mathbf{G}$  denotes the ZW generation matrix. The third step at the receiver consists in the equalization operation. To do the equalization, pseudo inverse of  $(\mathbf{H}\mathbf{G})$  has to be found, to have

$$\check{\mathbf{d}} = \mathbf{E} \tilde{\mathbf{y}} \quad (2.23)$$

where  $\mathbf{E}$  and  $\check{\mathbf{d}}$  are the estimator matrix and estimated data vector in the frequency domain, respectively. The Gauss-Markov theorem is applied on (2.22) with the noise covariance matrix  $C_{nn} = \mathbf{E}[\mathbf{n}'^H \mathbf{n}'] = L\sigma_n \mathbf{I}$ . Therefore, the Best Linear Unbiased Estimator (BLUE) is ([10]):

$$\mathbf{E} = (\mathbf{G}^H \mathbf{H}^H \mathbf{H} \mathbf{G})^\dagger \mathbf{G}^H \mathbf{H}^H. \quad (2.24)$$

In step four,  $\check{\mathbf{d}}$  is passed through an  $N$ -point IDFT to have the estimated data vector in the time domain:

$$\hat{\mathbf{d}} = \mathbf{D}_N^{-1} \check{\mathbf{d}}, \quad (2.25)$$

where  $\hat{\mathbf{d}}$  is the estimated data vector in the time domain. In the next part, we present different simulations to evaluate the performance of the proposed waveform.

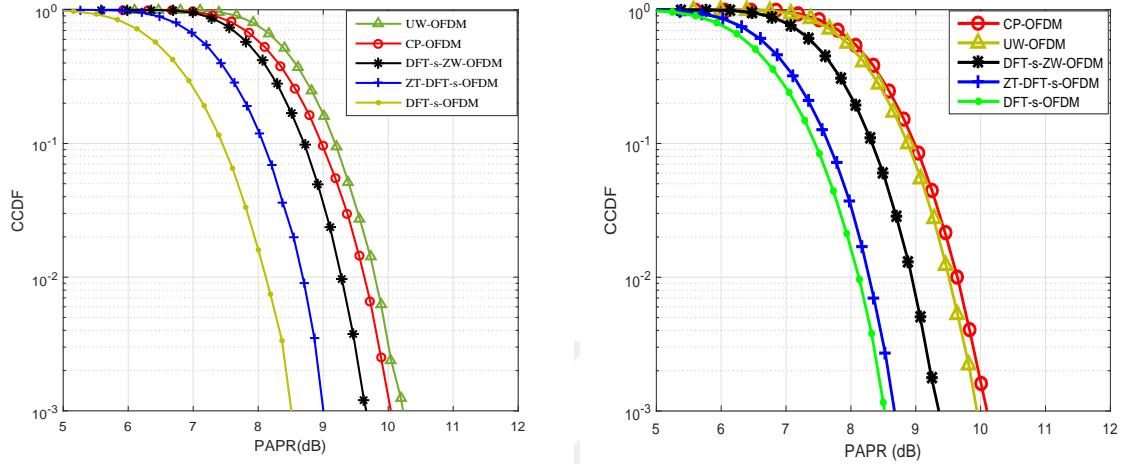


Fig. 2.5: PAPR comparison. [left:] with considering tails, [right:] without considering tails.

## 2.2 Performance Evaluation

In simulations, five important waveforms are compared with respect to five critical issues: time domain characteristics, PAPR, OOB emission, BER and transmitted symbol density.

**Simulation Parameters:** The simulations are done with QPSK modulation and  $L = 256$  is assumed as IFFT-size. Two users in uplink transmission are considered, each with DFT size equals to  $N = 100$ , resulting in  $2 \times 100 = 200$  as the total DFT size. The length of ZW, ZT and CP are set to be equal (CP=ZT=ZW,  $N_r = N_{zw} = 32$ ).

As the first comparison, different waveforms are compared in the time domain. Time samples of ZT DFT-s-OFDM, DFT-s-OFDM and the proposed waveform are shown in Fig. 2.3. In the proposed waveform due to zero word, difference between power of the tail and non-tail part is large enough that makes the scheme to perform outstandingly better than ZT DFT-s-OFDM in dispersive channels. CP-OFDM and DFT-s-OFDM use a CP to prevent ISI in dispersive channels, therefore they are less efficient in the time domain.

One of the important contributions is having guard interval with flexible length. As shown in Fig. 2.4 two CP-OFDM frames each with different CP size lead to different frame durations. In this situation, orthogonality between different

frames has been lost which leads to interference and degraded performance. On the contrary, the guard interval in DFT-s-ZW-OFDM is part of IFFT output which is the reason of having orthogonality with different lengths of guard interval.

As the second comparison, PAPR is considered. In terms of PAPR comparison, due to effect of the tails on it, two approaches are considered; one considers tails and the other one does not. Thanks to the new amplifier systems with the merit of switching quickly between different levels of power that results in having two or more linear operating ranges. Thus, the second approach presents the fair comparison between the schemes.

Both aspects in PAPR comparison according to CCDF curves of CP-OFDM, UW-OFDM, DFT-s-OFDM, ZT DFT-s-OFDM and the proposed waveform are shown in Fig. 2.5. The proposed model has around 0.7 dB better performance compared to CP-OFDM and UW-OFDM in Fig. 2.5. In simulations, localized mapping is considered like LTE-uplink standard. However, better results can be achieved by distributed mapping. DFT-s-OFDM and ZT-DFT-s-OFDM have better PAPR performance due to the pure data transmission. In UW-OFDM for fairness, adding unique word is not taken into account. In other words, unique word is assumed as zero word.

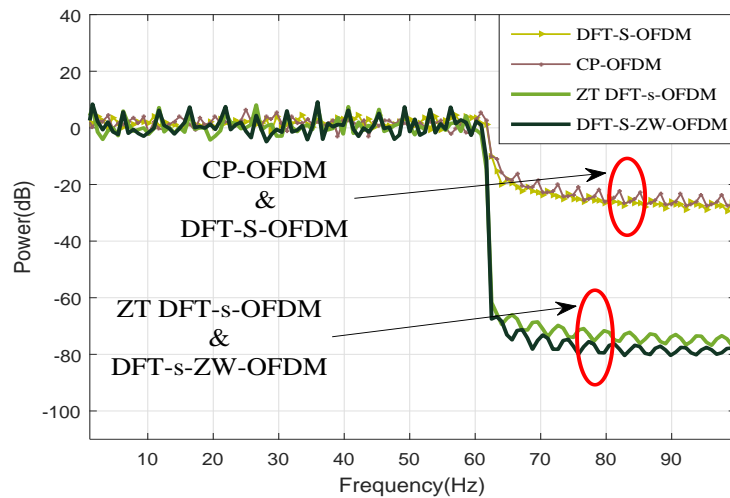


Fig. 2.6: Power spectral density comparison.

Evaluation of side lobes level is the third comparison. Having large sidelobes is another demerit of CP-OFDM and DFT-s-OFDM which makes the waveforms inappropriate for 5G. In simulation the edge subcarriers of all the waveforms are matched in order to have a fair comparison of OOB emission level. As shown in Fig. 2.6, power of side lobes of DFT-s-ZW-OFDM is extremely low about -60 dB less than CP-OFDM. In CP-OFDM due to its large OOB emission, a guard band is required between two resource blocks while in the proposed schemes there is no need for guard band as much as in CP-OFDM. In the proposed waveform due to adding redundant subcarriers the main lobe is wider than CP-OFDM but the good OOB emission can compensate the usage of redundancy in the frequency domain. Figs. 2.7 and 2.8 show the BER performance of the proposed

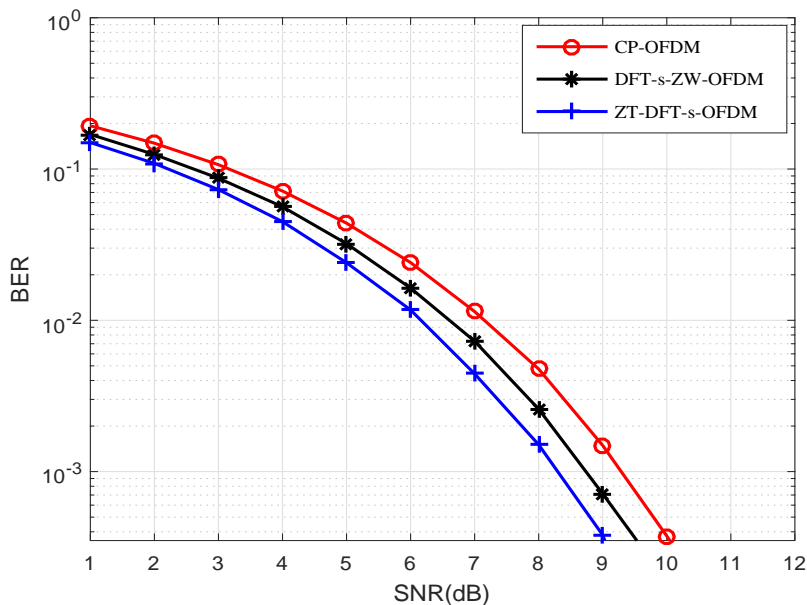


Fig. 2.7: BER comparison for the AWGN channel.

waveform in AWGN and Rayleigh fading multipath channels, respectively as the fourth comparison. As shown in Fig. 2.7, ZT DFT-s-OFDM and DFT-s-ZW OFDM outperform CP-OFDM in AWGN channel. The reason of the good performances is laid in power efficiency of the schemes. ZT DFT-s-OFDM signal has more power efficiency than the two others. It has neither CP nor redundant subcarriers. Redundant subcarriers in DFT-s-ZW-OFDM consumes more power than ZT DFT-s-OFDM but less than CP in CP-OFDM. Therefore the BER of DFT-s-ZW-OFDM is better than CP-OFDM.

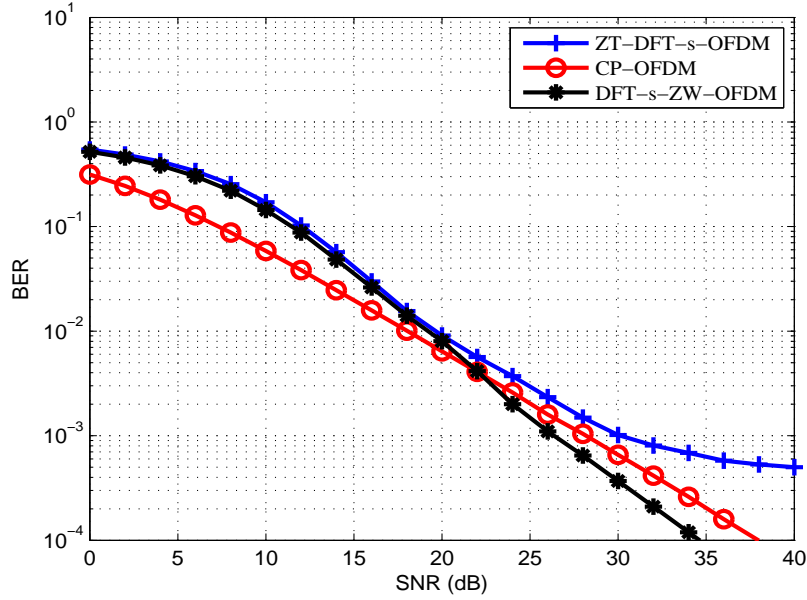


Fig. 2.8: BER comparison in Rayleigh fading channel.

BER performance in Rayleigh fading channel with uniform distribution power delay profile (PDP) and maximum delay spread  $\tau_{max} = N_{zw}$ , is shown in Fig. 2.8. ZT DFT-s-OFDM due to its tail power suffers from ISI, therefore it has higher BER, which is the reason for non decreasing curve in high SNRs. The proposed method outperforms CP-OFDM in BER performance around 3 dB.

Finally, the transmitted symbols are transmitted every  $T_{IFFT} + T_{CP}$  seconds in CP-OFDM and also spread along the frequency domain with frequency spacing of  $f = \frac{1}{T_{IFFT}}$ ; so data symbol density of CP-OFDM is defined as follow [7]

$$\eta_{\text{OFDM}} = \frac{T_{\text{IFFT}}}{T_{\text{IFFT}} + T_{\text{CP}}} = \frac{L}{L + N_{\text{CP}}} \leq 1, \quad (2.26)$$

where  $L$  is the size of IFFT and  $N_{\text{CP}}$  is the number of samples in CP. Similarly, in DFT-s-ZW-OFDM the data symbol density equals

$$\eta_{\text{DFT-s-ZW-OFDM}} = \frac{L - N_{zw}}{L}. \quad (2.27)$$

For the simulation parameters:

$$\eta_{\text{OFDM}} = \frac{256}{256 + 32} \approx 88.9\% \quad (2.28)$$



$$\eta_{\text{DFT-s-ZW-OFDM}} = \frac{256 - 32}{256} = 87.5\%. \quad (2.29)$$

As the fifth comparison, data symbol density in the proposed model is comparable with CP-OFDM as it is only about 1.4% less than it.

At the end, the comparisons are summarized in Table 2.1. All the mentioned waveforms are orthogonal in frequency domain due to IFFT characteristics.

Table 2.1: Comparison between various waveforms

	CP-OFDM	DFT-s-OFDM SC-FDM	UW-OFDM	ZT DFT-s OFDM	DFT-s-ZW -OFDM
Orthogonality	Orthogonal	Orthogonal	Orthogonal	Orthogonal	Orthogonal
PAPR	High	Low	High	Low	Low
CP	Yes	Yes	No	No	No
ISI problem	No	No	No	Yes	No
OOB emission	Bad	Bad	Good	Good	Good
Complexity	Low	Low	Normal	Low	Normal

## 2.3 Conclusions

In this paper, DFT-s-ZW-OFDM is presented as a new waveform candidate for 5G networks. Advantages of the proposed waveform are low PAPR and low OOB emission. Whereas the highlighted ones are its adaptivity in length of ZW and its superior BER performance in time dispersive channels. With the adaptivity that DFT-s ZW OFDM provides, different lengths of ZW can exist within the same resource block while the orthogonality is kept. This adaptivity along with the remarkable performances provided by acceptable complexity causes that DFT-s-ZW-OFDM outperforms other mentioned candidate waveforms.

# Chapter 3

## A Flexible Hybrid Waveform

The similarity between the transceivers of ZT DFT-s OFDM and DFT-s ZW OFDM helps to have a possibility of using the next to each other with a minor changes and creating a hybrid waveform. The hybrid waveform structure is explained as follows.

### 3.1 System Description and Properties

The hybrid method utilizes ZT DFT-s-OFDM and DFT-s-ZW OFDM in order to achieve high flexibility in power consumption with regard to the BER performance in multipath channels. In the following, descriptions about both waveforms are given. Then, the hybrid model is explained.

#### 3.1.1 Zero Tail DFT Spread OFDM

ZT DFT-s-OFDM is in the category of single carrier frequency division multiplexing (SC-FDM) schemes [5] (e.g. like DFT-s-OFDM [29]). It utilizes a group of redundant zeros to make a low power guard interval at the end of transmitted signal.

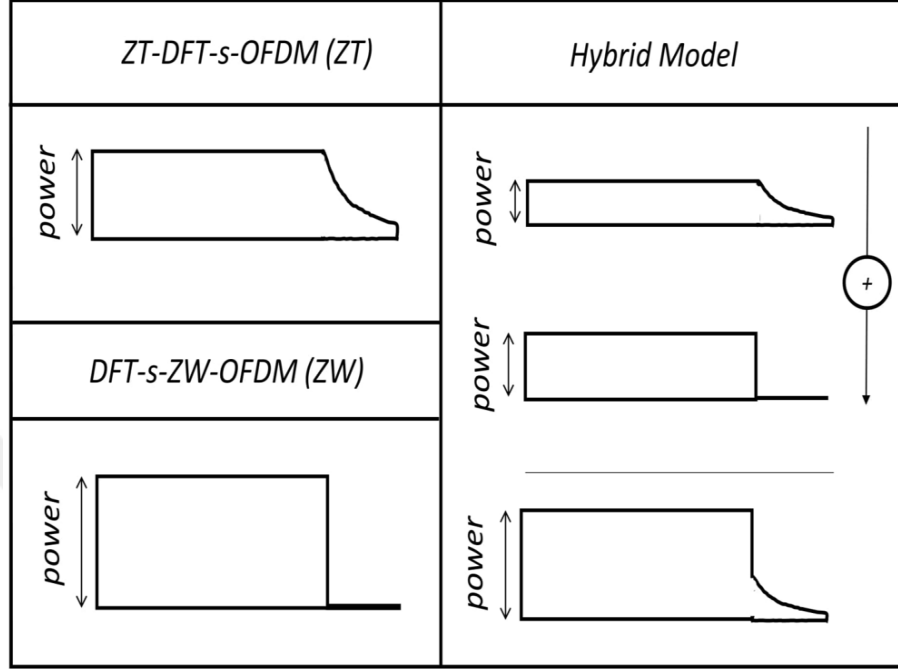


Fig. 3.1: Comparison of symbol power and tail power in ZT DFT-s OFDM, DFT-s ZW-OFDM and Hybrid model.

In a ZT DFT-s-OFDM, the column vector output signal denoted by  $\mathbf{x}_{zt}$  is expressed as

$$\mathbf{x}_{zt} = \mathbf{D}_L^{-1} \mathbf{B} \mathbf{D}_{(N_{zt}+N_{rz})} \begin{bmatrix} \mathbf{d}_{zt} \\ \mathbf{O}_{rz} \end{bmatrix}, \quad (3.1)$$

where  $\mathbf{d}_{zt}$  and  $\mathbf{O}_{rz}$  denote data and redundant zero vectors in time domain, respectively.  $\mathbf{D}$  denotes the square DFT matrix with size of  $(N_{zt} + N_{rz})$ .  $N_{zt}$  and  $N_{rz}$  indicate the number of data symbols and redundant zeros, respectively. Matrix  $\mathbf{B} \in \{0, 1\}^{L \times (N_{zt}+N_{rz})}$  maps the used and unused subcarriers.  $L$  is the size of square IDFT matrix  $\mathbf{D}^{-1}$  and  $L > N_{zt} + N_{rz}$ .

$\mathbf{x}_{zt}$  has a portion of low power guard interval known as zero tail; however, unlike its name, is an imperfect zero tail (Fig. 3.1). This low power tail causes to ISI problem in time dispersive channels.

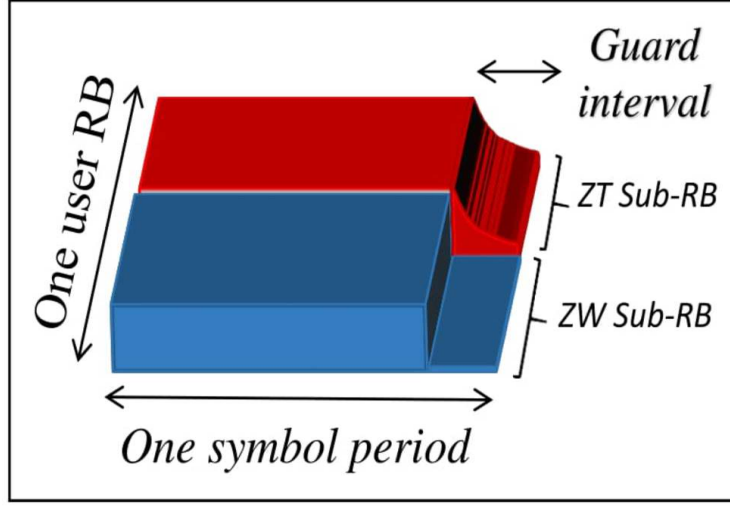


Fig. 3.2: Co-existence of two waveforms as two Sub-RBs with equal symbol periods and guard intervals.

### 3.1.2 DFT Spread Zero Word OFDM

DFT-s ZW OFDM is also a type of SC-FDM which utilizes a group of redundant subcarriers, similar to UW-OFDM [10], in order to nullify the tail of ZT DFT-s-OFDM. The transmitted signal denoted by  $\mathbf{x}_{zw}$  is defined as

$$\mathbf{x}_{zw} = \mathbf{D}_L^{-1} \mathbf{V} \mathbf{P} \begin{bmatrix} \mathbf{D}_{N_{zw}} \mathbf{d}_{zw} \\ \tilde{\mathbf{r}} \end{bmatrix}, \quad (3.2)$$

where  $\mathbf{d}_{zw}$  denotes the data vector in time domain.  $N_{zw}$  shows the length of the data vector. Redundant subcarriers vector shown by  $\tilde{\mathbf{r}}$ , is made by transformation matrix  $\mathbf{T}$ . All the redundant and data subcarriers are permuted by matrix  $\mathbf{P} \in \{0, 1\}^{(N_{zw}+N_{rw}) \times (N_{zw}+N_{rw})}$  and inserted in the desired positions by matrix  $\mathbf{V} \in \{0, 1\}^{L \times (N_{zw}+N_{rw})}$ . This waveform has better performance than ZT waveform in multipath channels. However, as shown in Fig. 3.1, DFT-s ZW OFDM requires more power compared to ZT DFT-s OFDM because the redundancy in DFT-s ZW OFDM requires power while redundancy in ZT DFT-s OFDM is only zeros without consuming power. In order to avoid confusion, we use ZW waveform and ZT waveform as the abbreviation of DFT-s ZW OFDM and ZT DFT-s-OFDM, respectively, in the rest of the paper.

### 3.1.3 Hybrid Model

Fig. 3.2 depicts the concept of the co-located waveforms in one RB in order to have flexibility in both the symbol power and tail power. As shown in Fig. 3.1, ZT waveform has less symbol power than ZW waveform; however, the ZT waveform contains more power in its tail than the ZW waveform.

Fig. 3.2 shows that the ZT waveform sub-RB and ZW waveform sub-RB are located next to each other without any guard band between two sub-RBs. The reason lies in the fact that both of the waveforms can use the same subcarrier frequency spacings next to each other without interfering to each other. As shown in Fig 3.3, due to using Sinc-shaped subcarriers with the same bandwidths, orthogonality between the two waveforms is kept. Moreover, none of them require additional guard interval in time domain, hence, with the same IDFT size, the symbol duration for both of them are the same. In the hybrid waveform, there

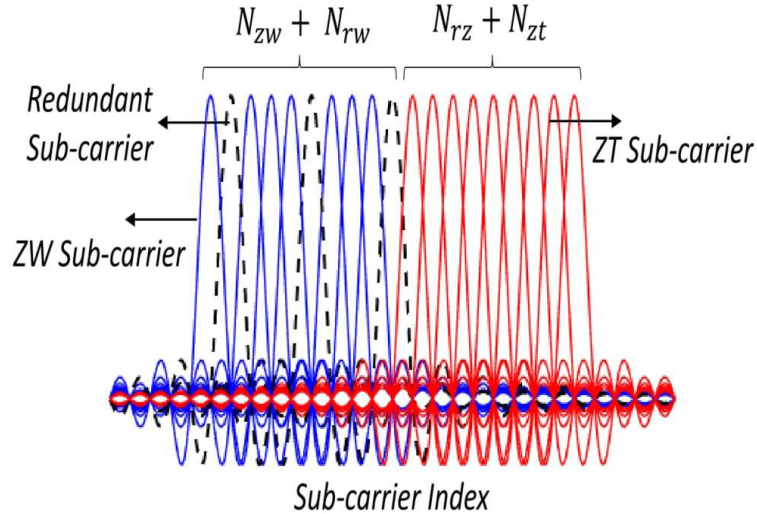


Fig. 3.3: Co-locating ZW and ZT subcarriers without a guard between them.

is a trade-off between having lower symbol power and lower tail power, in order to control the BER performance in time dispersive channels. In other words, this co-located waveform has the flexibility to adapt itself with the user requirement variation in cellular networks. For a user with the restriction of power consumption, more subcarriers can be dedicated to ZT waveform, whereas in highly dispersive channel, more subcarriers can be dedicated to ZW waveform.

## 3.2 Implementation and Complexity

The hybrid waveform implementation is based on the amount of dedicated resource elements to each waveform in order to obtain a flexible and low complex numerology. Signal transmission by hybrid waveform includes three steps. Figs. 3.4 and 3.5 depict the signal construction.

In step one, resource allocation decision (RAD) block in Fig. 3.4 decides about the division of the resource elements (subcarriers) between two waveforms with respect to the user requirements. It can get the necessary information from the cell where user is located in. It gives  $\alpha$  and  $\beta$  as the ratio of dedicated subcarriers to ZT and ZW waveforms over the total data subcarriers, respectively:

$$\begin{cases} \alpha = \frac{N_{zt}}{N_{zt}+N_{zw}} \\ \beta = \frac{N_{zw}}{N_{zt}+N_{zw}} \end{cases} \quad (3.3)$$

It is worth noting that  $\alpha + \beta = 1$ . When  $\alpha = 1, \beta = 0$  means the total system

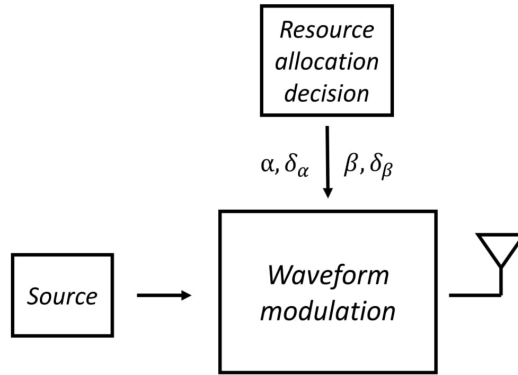


Fig. 3.4: Size of sub-RBs is controlled by resource allocation decision (RAD) block checking the user requirements.

is working as the ZT waveform and contrary, when  $\alpha = 0, \beta = 1$ , system serves as ZW waveform. Number of dedicated subcarriers to each waveform depends on the user requirement, (e.g., in rich scattered environments more subcarriers are allocated to ZW waveform compared to ZT waveform, however, in poor local scattered areas for having lower power consumption, ZT waveform takes more subcarriers). In case of redundancy, let  $\delta_\alpha$  and  $\delta_\beta$  denote the ratio of redundant

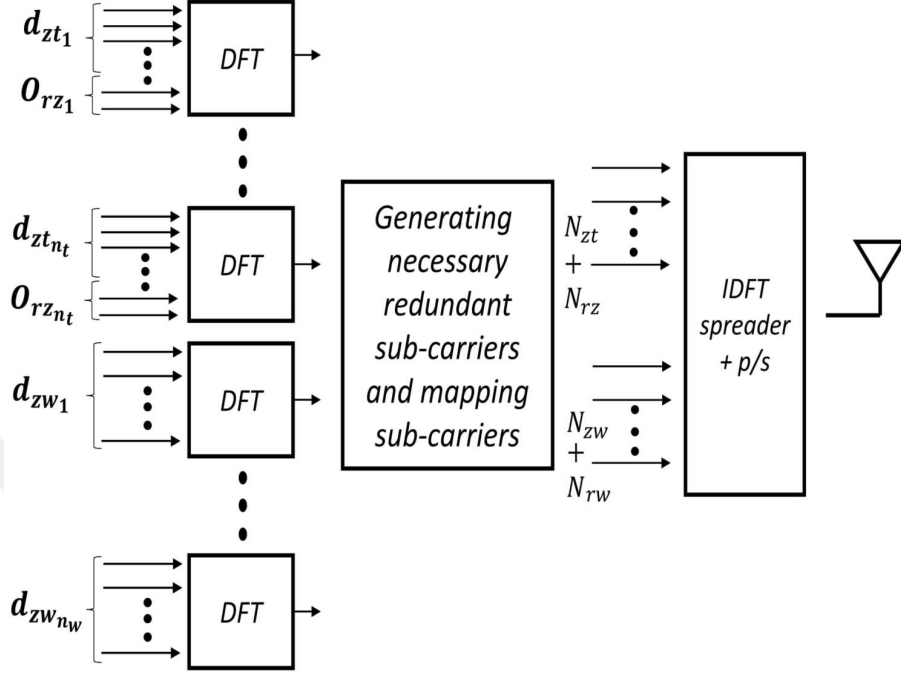


Fig. 3.5: Block diagram of the proposed hybrid waveform.

zeros and redundant subcarriers over the total redundancy, respectively.

$$\begin{cases} \delta_\alpha = \frac{N_{rz}}{N_{rw} + N_{rz}} \\ \delta_\beta = \frac{N_{rw}}{N_{rw} + N_{rz}}. \end{cases} \quad (3.4)$$

Changing the amount of redundancies has a direct relation with the number of dedicated data subcarriers. The more  $\alpha$ , the more  $\delta_\alpha$ , ( $\delta_\alpha + \delta_\beta = 1$ ). Another fact is that in ZW waveform the optimum case is  $N_{rw} = \text{length of tail}$  [10].

In the following, data is divided between ZT and ZW waveforms with respect to  $\alpha$  and  $\beta$  obtained from RAD block.

$$\mathbf{d}_{zt} = [\mathbf{d}_{zt_1}^T \mathbf{d}_{zt_2}^T \cdots \mathbf{d}_{zt_{n_t}}^T]^T, \quad (3.5)$$

$$\mathbf{d}_{zw} = [\mathbf{d}_{zw_1}^T \mathbf{d}_{zw_2}^T \cdots \mathbf{d}_{zw_{n_w}}^T]^T, \quad (3.6)$$

where  $\mathbf{d}_{zt}$  and  $\mathbf{d}_{zw}$  are the group of data assigned to ZT and ZW waveforms, respectively.  $\mathbf{d}_{zt}$  is divided into the  $n_t$  sub-groups and  $\mathbf{d}_{zw}$  into  $n_w$  sub-groups.

$\mathbf{d}_{zt_i}$  and  $\mathbf{d}_{zw_j}$  denote  $i^{th}$  and  $j^{th}$  sub-group, respectively.

For simplicity of implementation, we consider  $n_t + n_w$  DFT blocks as shown in Fig. 3.5. Data vectors in (3.5) and (3.6) are located as the input of these DFT units as shown in Fig. 3.5. Zero redundancy are appended to the end of the  $\mathbf{d}_{zt_i}$ s.

In step two, after data passed through DFT blocks, redundant subcarriers related to the  $\tilde{\mathbf{d}}_{zw}$  are appended in frequency domain. Mapping of subcarriers is done in this step by known matrices  $\mathbf{B}$  and  $\mathbf{V}$  same as (3.1) and (3.2). Fig. 3.3 shows a localized mapping distribution of subcarriers which provides multi-sub-RB scheduling gain in frequency domain.

In step three, all the mapped subcarriers are passed through an IDFT block as shown in the Fig. 3.5. By considering the explained changes and notations in (3.1) and (3.2) we have:

$$\mathbf{X} = \mathbf{D}_L^{-1} \left\{ \mathbf{B} \overbrace{\begin{bmatrix} \mathbf{D}_{\left(\frac{N_{zt} + N_{rz}}{n_t}\right)} \begin{bmatrix} \mathbf{d}_{zt_1} \\ \mathbf{O}_{rz_1} \end{bmatrix} \\ \mathbf{D}_{\left(\frac{N_{zt} + N_{rz}}{n_t}\right)} \begin{bmatrix} \mathbf{d}_{zt_2} \\ \mathbf{O}_{rz_2} \end{bmatrix} \\ \vdots \\ \mathbf{D}_{\left(\frac{N_{zt} + N_{rz}}{n_t}\right)} \begin{bmatrix} \mathbf{d}_{zt_{n_t}} \\ \mathbf{O}_{rz_{n_t}} \end{bmatrix} \end{bmatrix}}^{\mathbf{S}_{zt}} + \mathbf{VP} \underbrace{\begin{bmatrix} \mathbf{D}_{\frac{N_{zw}}{n_w}} \mathbf{d}_{zw_1} \\ \mathbf{D}_{\frac{N_{zw}}{n_w}} \mathbf{d}_{zw_2} \\ \vdots \\ \mathbf{D}_{\frac{N_{zw}}{n_w}} \mathbf{d}_{zw_{n_w}} \\ \tilde{\mathbf{r}} \end{bmatrix}}_{\mathbf{S}_{zw}} \right\}, \quad (3.7)$$

where  $\mathbf{X}$  is the transmitted signal. The size of DFT units are assumed to be the same. So, we can assume  $\frac{N_{zt}}{n_t} + \frac{N_{rz}}{n_t} = \frac{N_{zw}}{n_w} = k$ . This assumption maintain the complexity of hardware design as low as ZT and ZW waveforms.

The power of  $\mathbf{X}$  can be defined as:

$$E_x = \mathbf{E} \{ \mathbf{X}^H \mathbf{X} \}. \quad (3.8)$$



By substituting (3.7) in (3.8), we have:

$$\begin{aligned}
P_x &= \\
&\mathbf{E} \left\{ (\mathbf{D}_L^{-1}(\mathbf{B}\mathbf{S}_{zt} + \mathbf{VPS}_{zw}))^H (\mathbf{D}_L^{-1}(\mathbf{B}\mathbf{S}_{zt} + \mathbf{VPS}_{zw})) \right\} \\
&= \frac{1}{L} \mathbf{E} \left\{ ((\mathbf{B}\mathbf{S}_{zt})^H + (\mathbf{VPS}_{zw})^H) \mathbf{I} (\mathbf{B}\mathbf{S}_{zt} + \mathbf{VPS}_{zw}) \right\} \\
&= \frac{1}{L} \mathbf{E} \left\{ \mathbf{S}_{zt}^H \mathbf{I} \mathbf{S}_{zt} + \mathbf{S}_{zw}^H \mathbf{I} \mathbf{S}_{zw} \right\} \\
&= \frac{1}{L} \mathbf{E} \left\{ k \left( [\mathbf{d}_{zt_1}^H \ \mathbf{O}_{\mathbf{r}z_1}^H] \begin{bmatrix} \mathbf{d}_{zt_1} \\ \mathbf{O}_{\mathbf{r}z_1} \end{bmatrix} + \dots \right. \right. \\
&\quad \left. \left. + [\mathbf{d}_{zt_{n_t}}^H \ \mathbf{O}_{\mathbf{r}z_{n_t}}^H] \begin{bmatrix} \mathbf{d}_{zt_{n_t}} \\ \mathbf{O}_{\mathbf{r}z_{n_t}} \end{bmatrix} \right) + (k) \left( \mathbf{d}_{zw_1}^H \mathbf{d}_{zw_1} + \dots \right. \right. \\
&\quad \left. \left. + \mathbf{d}_{zw_{n_w}}^H \mathbf{d}_{zw_{n_w}} \right) + \tilde{\mathbf{r}}^H \tilde{\mathbf{r}} \right\} \\
&= \frac{1}{L} (kN_{zt}\sigma_{zt}^2 + kN_{zw}\sigma_{zw}^2 + \mathbf{E}\{\tilde{\mathbf{r}}^H \tilde{\mathbf{r}}\}), \tag{3.9}
\end{aligned}$$

where the  $\sigma_{zw}$  and  $\sigma_{zt}$  denote the variances of zero mean independent identical distributed data of ZW and ZT waveforms, respectively. The power of redundant subcarriers is explained in Chapter 2. So, assuming  $\sigma_{zt} = \sigma_{zw} = \sigma_d$  the total transmitted power is:

$$P_x = \frac{k\sigma_d^2}{L} (N_{zt} + N_{zw} + tr(\mathbf{T}\mathbf{T}^H)). \tag{3.10}$$

It is worth noting that the power consumption depends on the number of dedicated data to each waveform and redundant subcarriers which affects the  $tr(\mathbf{T}\mathbf{T}^H)$  [10], e.g., when the system experiences a low delay spread channel, the power consumption can decrease by decreasing the  $N_{zw}$  and increasing  $N_{zt}$ .

In the next Section the simulations depict the flexibility and performance of the hybrid model.

### 3.3 Numerical Results

In this Section, first, power evaluation of the system is considered. Second, the BER performance of the system as the result of the trade-off between the symbol power and tail power is evaluated. Third, OOB emission are examined. Finally, the PAPR performance of the system is discussed.

Simulations are done for QAM data symbols with IDFT size of  $L = 256$  and DFT size of  $k = 32$  (totally 8 DFT blocks). Guard interval length is 20 which equals to  $N_{rw}$ .  $\mathbf{O}_{rzi} = [0, 0]^T$  and the total redundant zeros are  $n_t \times 2$ , where  $n_t$  and  $n_w$  are controlled by RAD block.

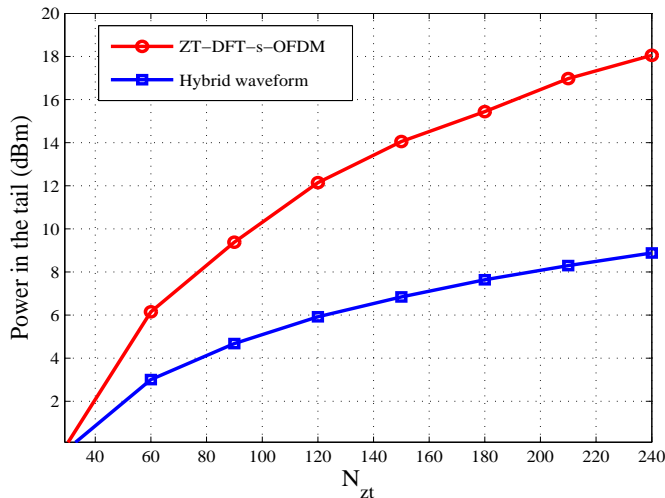


Fig. 3.6: Comparison of power in the tail of hybrid model and conventional ZT-DFT-s-OFDM. Tail power increases as  $N_{zt}$  increases.

#### 3.3.1 Power Evaluation

Fig. 3.6 compares the tail power in conventional ZT waveform with the proposed hybrid waveform. In simulations, for the conventional ZT waveform the remaining subcarriers (out of 256) are guard subcarriers while for hybrid waveform, remaining subcarriers are both ZW waveform and guard subcarriers. As shown in Fig. 3.6, tail power increases as  $N_{zt}$  increases. Hybrid waveform has 9dB lower power tail than ZT waveform when  $N_{zt} = 240$  due to using small DFT blocks rather than one DFT block in traditional ZT waveform.

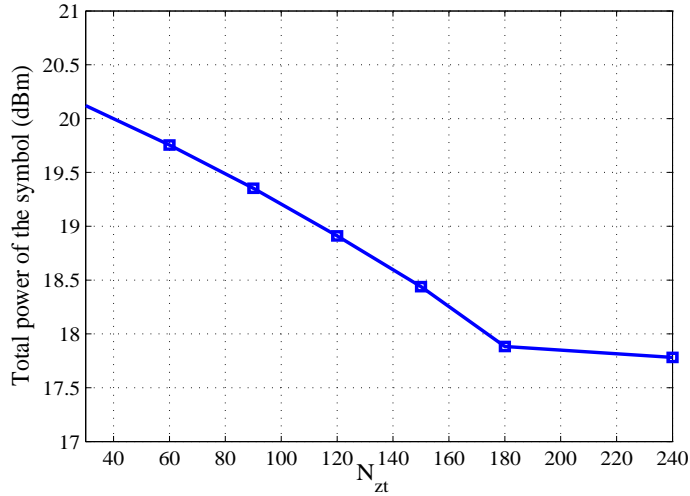


Fig. 3.7: Symbol power of hybrid model decreases as  $N_{zt}$  increases.

However, in spite of tail power by increasing the  $N_{zt}$ , the total symbol power in hybrid waveform decreases as shown in Fig. 3.7. The reason is that, as  $N_{zt}$  increases,  $\beta$  and the effect of ZW waveform is decreases. Figs. 3.6 and 3.7 show a trade-off between tail power and symbol power in the hybrid waveform.

### 3.3.2 Bit Error Rate

In order to show the BER performance of the hybrid waveform for different values of  $\alpha$  and  $\beta$ , a multipath Rayleigh fading channel with the uniform power delay profile (PDP) is considered. The maximum delay spread is  $\tau_{max} = \text{length of tail} + 1 = 21$ . Actual transmitted power for each curve is fixed. As shown in Fig. 3.8, hybrid waveform with smaller  $\alpha$  (larger  $\beta$ ) has better performance in high SNRs. Having larger  $\beta$  means dedicating more subcarriers to ZW waveform. However, in low SNRs because of power consumption of ZW waveform, BER performance of larger  $\alpha$  (smaller  $\beta$ ) is better. Thus, the crossing point of curves is the benchmark for RAD block to change  $\alpha$ ,  $\beta$  and their redundancies with respect to the SNR.

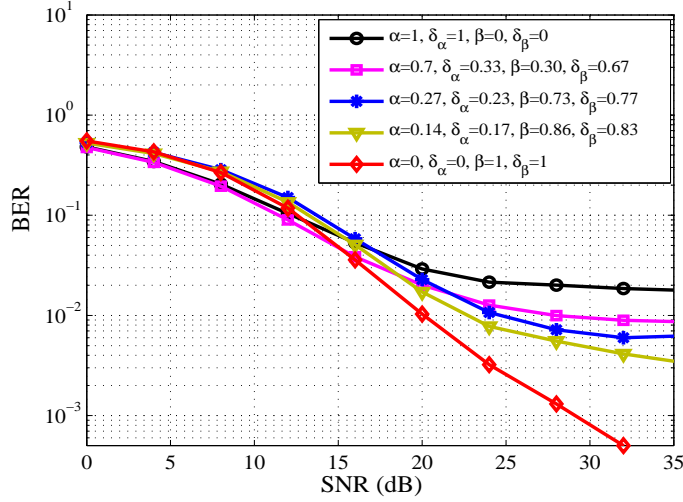


Fig. 3.8: BER performance of the hybrid waveform in Rayleigh fading channel with uniform PDP distribution,  $\tau = 21$ .

### 3.3.3 Out of Band Emission

Fig. 3.9 compares the power spectral density of the CP-OFDM and the proposed hybrid waveform for three different  $\alpha$  and  $\beta$  values. Both ZT and ZW waveforms have much lower OOB emission than CP-OFDM, thus the hybrid waveform also has a good OOB emission. Additionally, as shown in Fig. 3.9, by going from  $\alpha = 0$  toward  $\alpha = 1$  the ripples caused by redundant subcarriers is degraded. Therefore, tuning the  $\alpha$ ,  $\beta$  and their redundancies gives the high flexibility to be adapted with the spectral mask.

### 3.3.4 Peak to Average Power Ratio

In case of PAPR evaluation, PAPR performance of ZW waveform is dominant when  $0 \leq \alpha < 1$  which is given in. In other words, the peak-power of signal affected by ZW sub-RB is almost in the same ratio of average power. Only, when  $\alpha = 1$ , low PAPR is achieved.

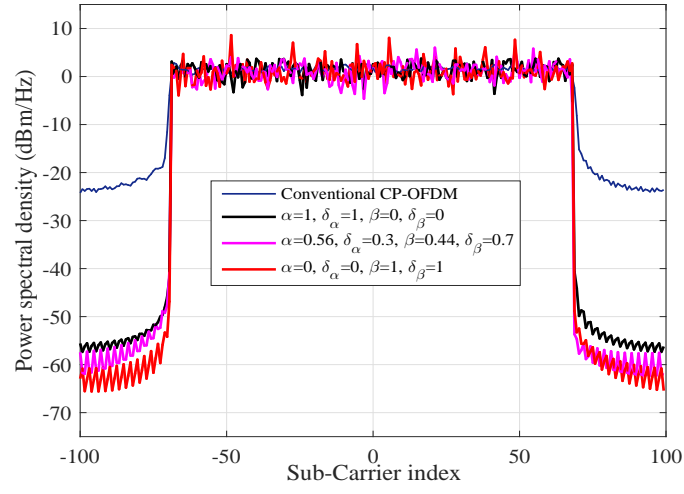


Fig. 3.9: Power spectral density comparison.

### 3.4 Conclusions and Future Research

The proposed hybrid waveform can change from strict ZT or ZW waveforms to a flexible hybrid waveform without using any extra guard band or guard interval.  $\alpha$  and  $\beta$  determine the output waveform characteristics. This variation in the output gives the ability to choose and change the desired waveform based on the user requirements. Flexibility, as one of the significant requirements for 5G waveform, is met in the proposed hybrid waveform.

# Chapter 4

## Low ICI Symbol Boundary Alignment

The Symbol boundary alignment has an important impact on the numerology design. The conventional LTE numerology, given in [30], is considered as a reference to propose the LICIS for the 5G numerology. Therefore, in the following, first, an overview of the conventional LTE symbol boundary alignment and its numerology design is given briefly and then the LICIS is explained in integration with that. The complexity of the LICIS is evaluated at end of this section.

### 4.1 Conventional Symbol Boundary Alignment Numerology

Fig. 4.1 shows the conventional LTE numerology, where the data is transmitted on the squeezed orthogonal subcarriers with the same unique subcarrier-spacing and symbol duration (including GI). Let  $\Delta f_s$  and  $T_\ell$  denote the reference subcarrier-spacing and symbol duration without GI, respectively. Moreover,  $\Delta f_s = \frac{\omega_s}{2} = \frac{1}{T_\ell}$  where  $\omega_s$  is the null to null bandwidth (BW) of each Sinc-shaped subcarrier. Each OFDM symbol, constructed by  $K$  subcarriers in one RB, is transmitted in one sub-slot with duration of  $T_\ell + T_{GI}$  where  $T_{GI}$  denote the GI

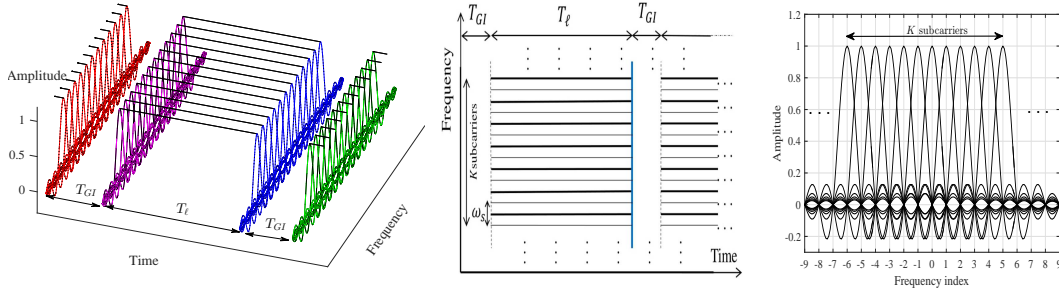


Fig. 4.1: Conventional LTE numerology as a reference numerology for LICIS.

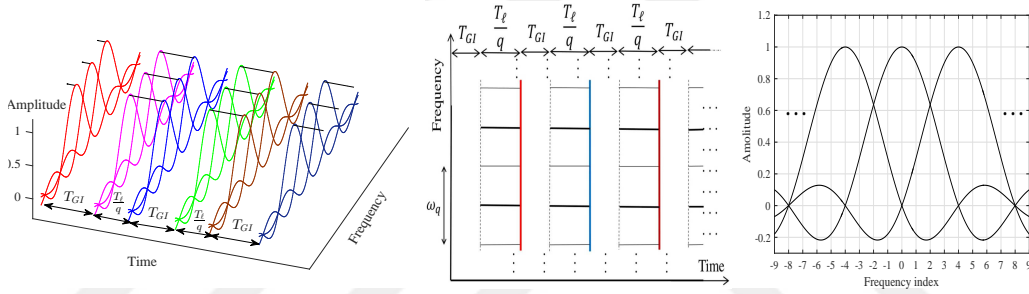


Fig. 4.2: Spectral inefficient numerology with large subcarrier-spacing and short symbol duration ( $\Delta f_q \sim \omega_q \rightarrow \frac{T_s}{q}$ ).

duration.  $K(= 12)$  subcarriers, with  $\Delta f_s(= 15 \text{ kHz})$ , build one RB and every 7 sub-slots, with normal GI length ( $\sim 4.7 \mu\text{s}$ ), construct one slot ( $=0.5\text{ms}$ ) [30]. Also, every two slots construct one transmission time interval (TTI=1 ms).

In the time and frequency dispersive channels, any small shifting of the orthogonal subcarriers, shown in Fig. 4.1, destroys the orthogonality of subcarriers and causes distortion as shown in Fig. 4.8. Therefore, the conventional LTE numerology is highly sensitive to the Doppler shift in high speed UAV communications.

In order to overcome the ICI problem, it has been discussed to use different fixed numerologies for different services in a single framework [31]. Particularly, the proposal focuses on using different scaled factor of reference subcarrier-spacing as

$$\Delta f_q = \Delta f_s \times \underbrace{2^m}_q, \quad m \in \{\mathbb{N} > 1\},$$

$$\frac{\Delta f_q}{\Delta f_s} = \frac{\omega_q}{\omega_s} = 2^m = q. \quad (4.1)$$

where the  $\Delta f_q$  and  $\omega_q$  denote the large subcarrier-spacing of the Sinc-shaped

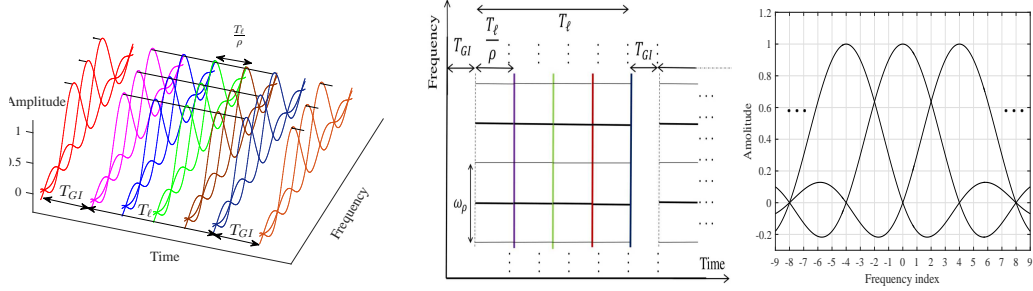


Fig. 4.3: LICIS structure.  $M$  OFDM symbols with  $\Delta f_\rho$  are inserted back to back and Only one GI exists at the end of them ( $M = \rho = 4$ ).

subcarriers and their null to null BW, respectively.  $m$  is an integer number greater than 1 ( $\mathbb{N}$  is the set of natural numbers) and  $q$  is the ratio of larger subcarrier-spacing over the reference subcarrier-spacing. Equation (4.1) is the rule of thumb for the scaled subcarrier-spacing ( $\Delta f_q$ ) based on the reference subcarrier-spacing ( $\Delta f_s$ ). Fig. 4.2 shows such a numerology. In fact, the larger  $\Delta f_q$  results in smaller OFDM symbol duration ( $T_q$ ) than coherence time ( $T_c$ ). Therefore, the time-variant channel is changed to the time-invariant channel for the system. However, by increasing the number of symbols in the time domain, a greater number of GI is required and consequently spectral efficiency is decreased.

## 4.2 Low ICI Symbol Boundary Alignment Numerology (LICIS)

Figs. 4.3 and 4.4 show the concept of LICIS where the  $M$  OFDM symbols, with large subcarrier-spacing of  $\Delta f_\rho$ , are inserted before one GI in a sub-slot. The sub-slot duration equals  $M\frac{T_\ell}{\rho} + T_{GI}$ . In LICIS, we have

$$\frac{\Delta f_\rho}{\Delta f_s} = \frac{\omega_\rho}{\omega_s} = \frac{T_\ell}{T_\rho} = \rho, \quad \rho \in \{\mathbb{N} > 1\}, \quad (4.2)$$

where  $\omega_\rho$  denotes the null to null BW of Sinc-shaped subcarriers in LICIS.  $T_\rho$  is the symbol duration corresponding to the  $\Delta f_\rho$  and  $\rho$  is the ratio of large



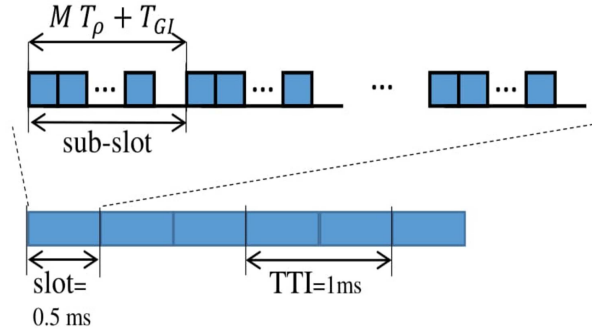


Fig. 4.4: Illustration of sub-slot, slot and TTI in LICIS. LICIS is based on the same reference clock as LTE.

subcarrier-spacing of LICIS over the reference subcarrier-spacing. Utilizing larger subcarrier-spacing decreases the effect of ICI problem in a given BW. Additionally, the smaller number of GI guarantees the spectral efficiency. Equation (4.2) assures that LICIS is based on the same reference clock as LTE because the integer and fraction frequency synthesizers offer a simple circuitual realization for synthesizing different frequencies based on the same common reference[27, 32]. It results in the compatibility of the LICIS with the current LTE numerology.

In LICIS, the orthogonality of the subcarriers is saved in the time-invariant channels properly as shown in Fig. 4.3. However, the multipath channel causes the ISI between the OFDM symbols in one sub-slot duration as shown in Fig. 4.5. The maximum delay spread of the channel, denoted by  $\tau_{\max}$ , is assumed to be less than the GI duration. Thus, there is no interference between different sub-slots. In order to remove the ISI inside one sub-slot, a pre-FFT multipath channel equalizer is applied on the whole received sub-slot and therefore, the major effect of time dispersion of wireless multipath fading channel can be removed.

### 4.2.1 Guard Interval Selection

Choosing a suitable GI has an important impact on the numerology design as well. CP and zero-padding (ZP) are the two dominant types of GI in OFDM [33]. Each method has its own advantages and disadvantages. For instance, CP requires more power consumption than ZP. Also, unlike CP-OFDM, ZP-OFDM

guarantees symbol recovery and assures FIR equalization of FIR channels regardless of the channel null locations [34, 35, 36]. However, ZP-OFDM requires more complex receiver. Authors in [34] propose a technique called ZP-FAST equalizer which has an acceptable complexity at the receiver side. In this study, due to utilizing the pre-FFT equalizer which is derived from ZP-FAST equalizer, ZP is considered as the GI. Additionally, by using the ZP, the duration of the loaded signal is  $MT_\rho$  which is shorter than  $MT_\rho + T_{GI}$  in the CP-used signal. It results in less ripples in power spectrum density (PSD) of the transmitted signal in ZP-OFDM and achieves better spectral mask efficiency.

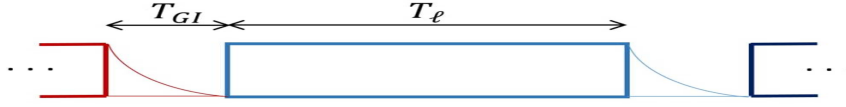


Fig. 4.5: Conventional symbol boundary alignment with  $\Delta f_s$  does not have ISI.

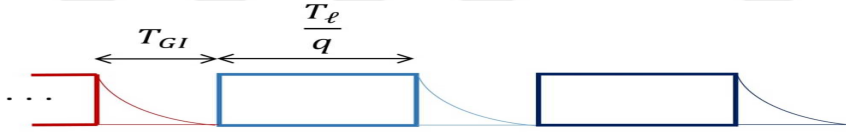


Fig. 4.6: Conventional symbol boundary alignment with  $\Delta f_q$  does not have ISI, ( $q = 2$ ).

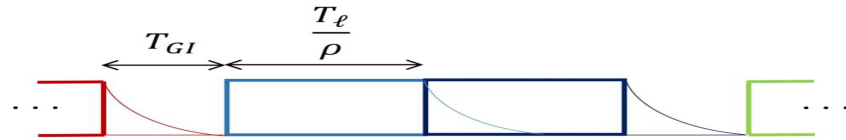


Fig. 4.7: LICIS has ISI inside one sub-slot ( $M = \rho = 2$ ).

#### 4.2.1.1 LICIS Construction

Let  $\tilde{\mathbf{d}}_\mu$  denote a stream of independent and identically distributed (i.i.d.) data symbols with zero mean and variance of  $\sigma_d^2$  for the  $\mu^{\text{th}}$  user in the frequency domain. Similar to the conventional LTE numerology,  $\tilde{\mathbf{d}}_\mu$  is divided into  $N_{RB}$  sub-streams with length of  $K$  and denoted by  $\tilde{\mathbf{d}}_{\mu,N}$  where  $N \in \{1, 2, \dots, N_{RB}\}$ . Therefore, the total number of used subcarriers equals  $R = K \times N_{RB}$ . Then we

have

$$\tilde{\mathbf{d}}_{\mu,N} \subset \tilde{\mathbf{d}}_{\mu} = [\tilde{\mathbf{d}}_{\mu,1}^T, \tilde{\mathbf{d}}_{\mu,2}^T, \dots, \tilde{\mathbf{d}}_{\mu,N_{RB}}^T]^T, \quad (4.3)$$

where  $(\cdot)^T$  represents transpose operation. The symbols of  $N^{\text{th}}$  RB are inserted in the desired subcarriers by matrix  $\mathbf{B}_N$ .  $\mathbf{B}_N \in \{0, 1\}^{\mathcal{L} \times K}$  is the mapping matrix for  $N^{\text{th}}$  RB where  $\mathcal{L} = MT_{\rho} = M \frac{T_{\ell}}{\rho}$ . The transmitted signal for the  $N^{\text{th}}$  RB denoted by  $\mathbf{X}_{\mu,N}$  is expressed as

$$\mathbf{X}_{\mu,N}^{\iota} = \mathcal{F} \mathbf{B}_N \tilde{\mathbf{d}}_{\mu,N}^{\iota}, \quad (4.4)$$

where  $\iota$  denotes the  $\iota^{\text{th}}$  sub-slot with length of  $\mathcal{L} + T_{GI}$  including  $M$  OFDM symbols with subcarrier-spacing of  $\Delta f_{\rho}$  and one GI. Matrix  $\mathcal{F}$  in (4.4) is expressed as

$$\mathcal{F} = \begin{bmatrix} \mathbf{F}_{T_{\rho}}^{-1} & \mathbf{O}_{T_{\rho}} & \cdots & \mathbf{O}_{T_{\rho}} \\ \mathbf{O}_{T_{\rho}} & \mathbf{F}_{T_{\rho}}^{-1} & \cdots & \mathbf{O}_{T_{\rho}} \\ \vdots & \ddots & \ddots & \vdots \\ \mathbf{O}_{T_{\rho}} & \cdots & \cdots & \mathbf{F}_{T_{\rho}}^{-1} \\ \mathbf{O}_{T_{GI}} & \cdots & \cdots & \mathbf{O}_{T_{GI}} \end{bmatrix}_{(\mathcal{L}+T_{GI}) \times \mathcal{L}} \quad (4.5)$$

where  $\mathbf{F}^{-1}$  and  $\mathbf{O}$  denote the IFFT and zero matrices, respectively. The indices at the bottom right of each matrix notation are the size of that square matrix meaning number of rows and columns. The last  $T_{GI}$  rows insert zero samples as a ZP (GI) at the end of sub-slot.

Eventually, the transmitted signal for the  $\mu^{\text{th}}$  user (utilizing  $R$  subcarriers in total) is derived as

$$\mathbf{X}_{\mu}^{\iota} = \mathcal{F} \underbrace{\sum_{N=1}^{N_{RB}} \mathbf{B}_N \tilde{\mathbf{d}}_{\mu,N}^{\iota}}_{\mathbf{P} \tilde{\mathbf{d}}_{\mu}^{\iota}} = \mathcal{F} \mathbf{P} \tilde{\mathbf{d}}_{\mu}^{\iota}. \quad (4.6)$$

In (4.6), matrix  $\mathbf{P} = [\mathbf{B}_1, \mathbf{B}_2, \dots, \mathbf{B}_{N_{RB}}]$  is defined for simplifying the notations. The duration of  $\mathbf{X}_{\mu}^{\iota}$  equals  $T_{\iota} = \mathcal{L} + T_{GI} = MT_{\rho} + T_{GI}$ .

### 4.2.1.2 Channel model

The transmitted signal given in (4.6) passes through a time and frequency dispersive channel and reaches to the receiver. The received signal corresponding to the  $\mathbf{X}_\mu$  is

$$\mathbf{Y}_\mu[n] = \sum_{\nu=0}^L h_\nu[n] \mathbf{X}_\mu[n - \tau_\nu] (e^{-j2\pi f_{d_\nu} n}) (e^{-j2\pi f_\delta n}) + \mathbf{w}[n], \quad (4.7)$$

where  $L$ ,  $h_\nu$ ,  $\tau_\nu$ ,  $f_{d_\nu}$ ,  $f_\delta$ , and  $\mathbf{w}$  denote the number of paths, complex quantity of the time based channel impulse of  $\nu^{\text{th}}$  path, delay of  $\nu^{\text{th}}$  path, Doppler shift of the  $\nu^{\text{th}}$  path, CFO of the system, and zero mean additive white Gaussian noise (AWGN) with the variance of  $\sigma_n^2$ , respectively. If we translate (4.7) into a matrix form for the  $i^{\text{th}}$  received sub-slot, we have

$$\mathbf{Y}_\mu^i = \overbrace{\mathbf{H}^i \mathbf{D}^i \mathbf{C}^i}^{\mathcal{H}^i} \mathbf{X}_\mu^i + \mathbf{W}^i, \quad (4.8)$$

where  $\mathcal{H}^i$  represents the  $T_i \times T_i$  matrix of time and frequency dispersive channel for the  $i^{\text{th}}$  sub-slot.  $\mathcal{H}^i$  is a contribution of  $\mathbf{H}^i$ ,  $\mathbf{D}^i$ , and  $\mathbf{C}^i$  representing the multipath channel, Doppler shift and CFO matrices, respectively.

$\mathbf{H}^i$  in (4.8) represents the  $T_i \times T_i$  lower triangular Toeplitz matrix of multipath channel modeled as a FIR filter with a channel impulse response of  $\mathbf{h} = [h_0, h_1, \dots, h_L]^T$  in the time domain. It is worth noting that during one sub-slot of signal transmission and without the Doppler effect, the multipath channel impulse response is assumed to be fixed. It means that the power delay profile (PDP) of the multipath channel for  $\mathbf{X}_\mu^i$  is fixed. This assumption is mandatory for circularity assumption of the multipath channel within duration of  $i^{\text{th}}$  sub-slot ( $T_i$ ) in the absence of the Doppler effect. In other words, the frequency dispersive

channel is caused only by the Doppler effect. Therefore, we have

$$\mathbf{H}^z = \begin{bmatrix} \overbrace{h_0 \quad 0 \quad \cdots \quad 0}^{\mathbf{H}_d} & \overbrace{0 \quad \cdots \quad 0}^{\mathbf{H}_{zp}} \\ h_1 \quad \ddots \quad \ddots \quad \vdots & 0 \quad \cdots \quad \vdots \\ \vdots \quad \ddots \quad \ddots \quad 0 & \vdots \quad \ddots \quad 0 \\ h_L \quad \cdots \quad h_1 \quad h_0 & 0 \quad \cdots \quad 0 \\ 0 \quad \ddots \quad \ddots \quad h_1 & h_0 \quad \cdots \quad 0 \\ \vdots \quad \ddots \quad \ddots \quad \vdots & \vdots \quad \ddots \quad \vdots \\ 0 \quad \cdots \quad 0 \quad h_L & h_{L-1} \quad \cdots \quad h_0 \end{bmatrix}_{T_i \times T_i}. \quad (4.9)$$

Regarding to the first  $\mathcal{L}$  columns of  $\mathbf{H}^z$ , the submatrix  $\mathbf{H}_d$  is a Toeplitz matrix ( $\mathcal{L}$  full-rank matrix) and is always guaranteed to be invertible, which assures symbol recovery regardless of the channel zero locations [34, 35, 36]. It is worth noting that  $\mathbf{H}_d$  is multiplied by the non-zero part of the  $\mathbf{X}_\mu^z$  while  $\mathbf{H}_{zp}$  is multiplied by the zero portion of  $\mathbf{X}_\mu^z$  and the result equals zero. Therefore, the circularity assumption of the multipath channel is obtained as

$$\mathbf{H}_c^z = \begin{bmatrix} \overbrace{h_0 \quad 0 \quad \cdots \quad 0}^{\mathbf{H}_d} & \overbrace{h_{L-1} \quad \cdots \quad h_1}^{\mathbf{H}_{zp}} \\ h_1 \quad \ddots \quad \ddots \quad \vdots & 0 \quad \ddots \quad \vdots \\ \vdots \quad \ddots \quad \ddots \quad 0 & \vdots \quad \ddots \quad h_{L-1} \\ h_L \quad \cdots \quad h_1 \quad h_0 & 0 \quad \cdots \quad 0 \\ 0 \quad \ddots \quad \ddots \quad h_1 & h_0 \quad \cdots \quad 0 \\ \vdots \quad \ddots \quad \ddots \quad \vdots & \vdots \quad \ddots \quad \vdots \\ 0 \quad \cdots \quad 0 \quad h_L & h_{L-1} \quad \cdots \quad h_0 \end{bmatrix}, \quad (4.10)$$

where  $\mathbf{H}_c^z$  is a circularized matrix form of  $\mathbf{h}$  vector when  $\tau_{\max} \leq T_{GI}$ .  $\mathbf{D}^z$ , in (4.8), denotes the  $T_i \times T_i$  lower triangular matrix which creates the Doppler effect in the channel. The Doppler effect in the frequency dispersive channel is modeled as Doppler shift denoted by  $f_{d_\nu}$  for  $\nu^{\text{th}}$  path. Similar to [37]

$$f_{d_\nu} = \frac{V_\mu}{V_s} f_k \cos\theta_\nu, \quad (4.11)$$

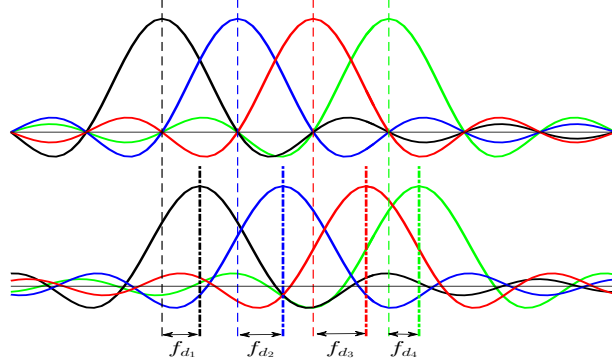


Fig. 4.8: The effect of Doppler shift over OFDM sub-carriers.

where  $V_\mu$ ,  $V_s$ ,  $f_k$ , and  $\theta_\nu$  represent the relative velocity, RF velocity, bandpass frequency of  $k^{\text{th}}$  subcarrier and path angle, respectively. It is worth noting that the Doppler effect is a combination of Doppler shift and Doppler spread. However, in high speed UAV communications, increasing the  $V_\mu$  causes to have larger Doppler shift than Doppler spread. Fig. 4.8 illustrates the effect of Doppler shift over OFDM subcarriers[37]. Additionally, we assume an unknown  $V_\mu$  which varies in a real environment. Thus, there are different Doppler shifts at each time instance due to the variation of  $V_\mu$ . In other words, for  $\nu^{\text{th}}$  path, Doppler shift can be different at each time instances. Therefore, the total number of Doppler shifts which exist in one sub-slot is set as  $\mathcal{Z}$ . Then based on (4.8) and (4.9), we have

$$\mathbf{H}^\nu \mathbf{D}^\nu = \begin{bmatrix} h_0 \Gamma^{f_{d_0}} & 0 & \dots & \dots & 0 \\ h_1 \Gamma^{f_{d_1}} & h_0 \Gamma^{f_{d_{L+1}}} & \ddots & \ddots & \vdots \\ \vdots & \ddots & \ddots & \ddots & \vdots \\ h_L \Gamma^{f_{d_L}} & \ddots & \ddots & \ddots & 0 \\ 0 & h_L \Gamma^{f_{d_{2L+1}}} & \ddots & \ddots & \vdots \\ \vdots & 0 & \ddots & \ddots & \vdots \\ \vdots & \ddots & \ddots & \ddots & \vdots \\ 0 & \dots & \dots & \dots & h_0 \Gamma^{f_{d_{\mathcal{Z}-1}}} \end{bmatrix} \quad (4.12)$$

where  $\Gamma = e^{-j2\pi}$ . Based on (4.8), (4.9), and (4.12), matrix  $\mathbf{D}^\nu$  can be written as  $\mathbf{D}^\nu = \mathbf{H}^{\nu \dagger} \mathcal{H}^\nu \mathbf{C}^{\nu^{-1}}$  where  $(\cdot)^\dagger$  represents pseudoinverse operation.

Matrix  $\mathbf{C}^i$  in (4.8) is defined as the diagonal CFO matrix affecting all subcarriers equally. The entries on the diagonal of matrix  $\mathbf{C}^i$  are assumed as the average frequency offset of the transceiver and are defined based on  $\Delta f_s = \frac{1}{T_\ell}$  as follows:

$$f_\delta = \frac{\delta}{T_\ell} = \delta \Delta f_s, \quad \delta \in [-1, 1], \quad (4.13)$$

where  $f_\delta$  is a fraction of reference subcarrier-spacing of  $\Delta f_s$ . Finally, the channel can be modeled as

$$\mathcal{H}^i = \mathbf{H}^i \mathbf{D}^i \mathbf{C}^i = \begin{bmatrix} h_0 \Gamma^{f_{d_0} + f_\delta} & 0 & \cdots & \cdots & 0 \\ h_1 \Gamma^{f_{d_1} + f_\delta} & h_0 \Gamma^{f_{d_{L+1}} + f_\delta} & \ddots & \ddots & \vdots \\ \vdots & \ddots & \ddots & \ddots & \vdots \\ h_L \Gamma^{f_{d_L} + f_\delta} & \ddots & \ddots & \ddots & 0 \\ 0 & h_L \Gamma^{f_{d_{2L+1}} + f_\delta} & \ddots & \ddots & \vdots \\ \vdots & 0 & \ddots & \ddots & \vdots \\ \vdots & \ddots & \ddots & \ddots & \vdots \\ 0 & \cdots & \cdots & \cdots & h_0 \Gamma^{f_{d_{Z-1}} + f_\delta} \end{bmatrix} \quad (4.14)$$

Substituting (4.10) into the (4.14) results in  $\mathcal{H}^i = \mathbf{H}_c^i \mathbf{D}^i \mathbf{C}^i$  and the received signal at (4.8) can be re-expressed as

$$\mathbf{Y}_\mu^i = \mathbf{H}_c^i \mathbf{D}^i \mathbf{C}^i \mathbf{X}_\mu^i + \mathbf{W}^i. \quad (4.15)$$

#### 4.2.1.3 Data Recovery in LICIS

Fig. 4.9 shows the data block diagram of the LICIS using zero forcing (ZF) equalizer.  $\mathbf{Y}_\mu^i$ , defined in (4.15), is the received vector which goes through a FFT block. The FFT-size of this FFT block equals the length of  $i^{\text{th}}$  sub-slot ( $T_i$ ). By assuming that the multipath channel state information is available at the receiver and similar to the case of ZP-FAST, studied in [34], for  $M$  OFDM symbols in

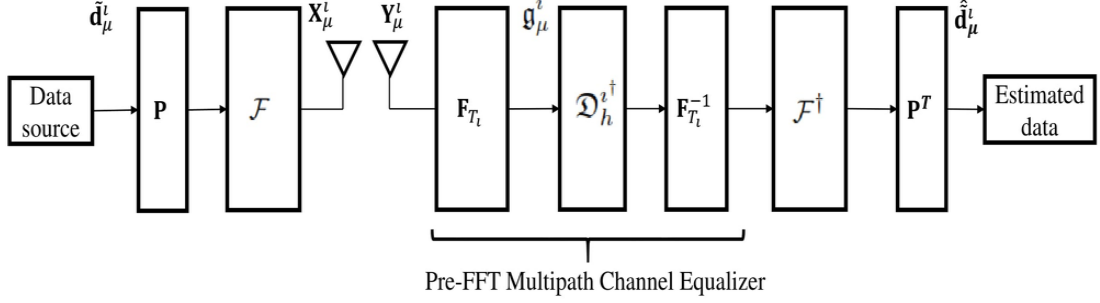


Fig. 4.9: Transmitter and receiver block diagram of the LICIS.

one sub-slot, we have

$$\mathbf{F}_{T_i} \mathbf{Y}_\mu^i = \underbrace{\mathfrak{D}_h^i}_{\mathbf{F}_{T_i} \mathbf{H}_c^i \mathbf{F}_{T_i}^{-1}} \mathbf{F}_{T_i} \mathbf{D}^i \mathbf{C}^i \mathcal{F} \mathbf{P} \tilde{\mathbf{d}}_\mu^i + \underbrace{\tilde{\mathcal{W}}^i}_{\mathbf{F}_{T_i} \mathbf{W}^i}, \quad (4.16)$$

where  $\mathfrak{D}_h^i$  is the  $T_i \times T_i$  diagonal matrix of frequency response of the multipath channel. In the frequency domain, the major effect of multipath channel is removed by a FDE (ZF equalization is done in the frequency domain), and then an IFFT transforms the signal into the time domain again

$$\underbrace{\mathcal{V}^i}_{\mathbf{F}_{T_i}^{-1} \mathfrak{D}_h^{i\dagger}} \underbrace{\mathfrak{g}_\mu^i}_{\mathbf{F}_{T_i} \mathbf{Y}_\mu^i} = \mathbf{D}^i \mathbf{C}^i \mathcal{F} \mathbf{P} \tilde{\mathbf{d}}_\mu^i + \mathbf{F}_{T_i}^{-1} \mathfrak{D}_h^{i\dagger} \tilde{\mathcal{W}}^i. \quad (4.17)$$

This is the process of the pre-FFT multipath equalizer. Also, by assuming that Doppler shifts and CFO are unknown, the result of  $\mathbf{D}^i \mathbf{C}^i$  is set as an identity matrix ( $\mathbf{I}_{T_i}$ ). Although estimation of  $\mathbf{D}^i$  and  $\mathbf{C}^i$  can improve the system performance, the complexity of the equalizer will be increased as well. So, we have

$$\mathcal{V}^i \mathfrak{g}_\mu^i = \mathbf{I}_{T_i} \mathcal{F} \mathbf{P} \tilde{\mathbf{d}}_\mu^i + \mathcal{V}^i \tilde{\mathcal{W}}^i. \quad (4.18)$$

Finally, the recovered data is

$$\hat{\mathbf{d}}_\mu^i = \mathbf{P}^T \mathcal{F}^\dagger \mathcal{V}^i \mathfrak{g}_\mu^i + \mathbf{P}^T \mathcal{F}^\dagger \mathcal{V}^i \tilde{\mathcal{W}}^i, \quad (4.19)$$

where  $\hat{\mathbf{d}}_\mu^i$  is the estimated data symbol stream in  $i^{\text{th}}$  sub-slot for the  $\mu^{\text{th}}$  user. It



is worth noting that the result of  $\mathcal{F}^\dagger \mathcal{V}^z$  is a  $\mathfrak{L}$  full-rank matrix. It guarantees the ZF symbol recovery, regardless of the channel nulls (like in [34]).

In order to avoid noise enhancement in ZF equalizer, a LMSE estimation can be deployed as

$$\hat{\mathbf{d}}_\mu^z = \mathbf{P}^T \mathcal{F}^H \mathbf{F}_{T_i}^H \mathcal{D}^{zH} \left[ \frac{\sigma_n^2}{\sigma_d^2} \mathbf{I}_{T_i} + \mathcal{D}_h \mathbf{F}_{T_i} \mathcal{F} \mathcal{F}^H \mathbf{F}_{T_i}^H \mathcal{D}_h^H \right]^{-1} \mathfrak{g}_\mu^z, \quad (4.20)$$

where  $(.)^H$  represents conjugate transpose operation. It is worth noting that the LMSE estimations, in both LICIS and conventional LTE numerologies, are relatively more complex than ZF.

## 4.2.2 Complexity Analysis

Relaxing the constraint of unique subcarrier-spacing for the 5G numerology design has not been standardized yet. However, an extensive discussion, in the literature (e.g., [27, 26, 38]), has been done to prove that it is a low complex candidate among the presented solutions for reducing ICI. The main disadvantage of using large subcarrier-spacing is its spectral inefficiency. Furthermore, using the large subcarrier-spacing only for high speed users and small subcarrier-spacing for low speed users leads to different symbol durations. It changes the synchronous transmission to an asynchronous transmission. It is evident that handling the asynchronous communications has its own complex solutions (e.g., filtering each user-RB like in [22]). Regarding to these issues, LICIS provides an opportunity to use the large subcarrier-spacing transmission in a sub-slot duration for both high and low speed users without losing spectral efficiency. In other words, the proposed approach facilitates the synchronous transmission for high and low speed users. The only complexity increment of the LICIS, compared to the conventional LTE numerology, is an additional FFT and IFFT operations for the equalizer. They are the  $\mathbf{F}_{T_i}$  and  $\mathbf{F}_{T_i}^{-1}$  matrices given in (4.17).

It is worth noting that the block of  $\mathcal{F}$  is as complex as one IFFT block with the size of  $\mathcal{L}$  in the conventional LTE numerology. Therefore, it does not increase the complexity of the system. Table 4.1 shows the fair complexity comparison in terms of FFT and IFFT blocks in the transceivers of conventional LTE numerology and LICIS. Moreover, in case of channel estimation, the same multipath channel estimation as conventional LTE numerology is required because the Doppler shift is not estimated in LICIS and multipath channel in absence of Doppler effect is assumed to be fixed during a sub-slot duration.

Table 4.1: Complexity comparison of transceivers in conventional LTE numerology and LICIS ( $M = \rho \Rightarrow T_\ell = \mathcal{L} = \rho T_\rho$ ).

	Conventional LTE numerology	LICIS
Transmitter	one IFFT block with size of $\mathcal{L}$	$\rho$ IFFT blocks with size of $\frac{\mathcal{L}}{\rho}$ ( $\mathcal{F}$ )
Receiver	one FFT block with size of $\mathcal{L}$	$\rho$ FFT blocks with size of $\frac{\mathcal{L}}{\rho}$ one FFT block with size of $T_i$ one IFFT block with size of $T_i$

### 4.3 Spectral Efficiency Analysis

In the case of spectral efficiency evaluation, the number of data bits, transmitted in the time domain, is considered as a metric called data bit density (like in [39]). The data bit density of three different scenarios are compared analytically as

follows:

- 1 Conventional numerology with reference subcarrier-spacing ( $\Delta f_s$ ) (e.g., Fig. 4.1)
- 2 Conventional numerology with large subcarrier-spacing ( $\Delta f_q$ ) (e.g., Fig. 4.2)
- 3 LICIS with subcarrier-spacing of  $\Delta f_\rho$  (e.g., Fig. 4.3)

The same GI duration is considered in all three scenarios. It is a fraction of  $T_\ell$  where  $T_{GI} = \frac{T_\ell}{\kappa}$ ,  $\kappa \in \{\mathbb{N} > 1\}$ . The given BW is fixed for all the scenarios as well.

In scenario 1, the data symbols of one RB are transmitted in sub-slot duration of  $T_\ell + T_{GI}$ . Thus, data bit density, denoted by  $\eta_1$ , is as follows

$$\eta_1 = \frac{K \times \log_2 \Lambda}{\left(\frac{K}{2}\omega_s\right)\left(T_\ell + \frac{T_\ell}{\kappa}\right)}, \quad (4.21)$$

where  $\Lambda$  denotes the modulation order of the symbols. In scenario 2, the data symbols of one RB are transmitted in sub-slot duration of  $\frac{T_\ell}{q} + T_{GI}$ . Therefore, we have

$$\eta_2 = \frac{\frac{K}{q} \times \log_2 \Lambda}{\left(\frac{K}{2q}\omega_q\right)\left(\frac{T_\ell}{q} + \frac{T_\ell}{\kappa}\right)}. \quad (4.22)$$

Finally for the LICIS, the data symbols of one RB are transmitted in sub-slot duration of  $M T_\rho + T_{GI}$  which leads to have

$$\eta_3 = \frac{M \frac{K}{\rho} \times \log_2 \Lambda}{\left(\frac{K}{2\rho}\omega_\rho\right)\left(M \frac{T_\ell}{\rho} + \frac{T_\ell}{\kappa}\right)}. \quad (4.23)$$

Increasing  $\Delta f_q$  in scenario 2 causes to decrease the symbol transmission duration. Thus, scenario 2 requires more GI than scenario 1 in a certain time period. Therefore, it is obvious that  $\eta_1 > \eta_2$ . The data symbol density of LICIS depends on  $M$ . Moreover,  $M$  depends on the period of time while the multipath channel is fixed, in absence of the Doppler effect, because the circularity assumption of the multipath channel in (4.10) is required to be satisfied during one sub-slot

duration. Thus, we have

$$\begin{cases} M \geq \rho & \Rightarrow \eta_3 \geq \eta_1 \\ M \geq \frac{\rho}{q} & \Rightarrow \eta_3 \geq \eta_2 \end{cases}. \quad (4.24)$$

In conventional numerologies, the multipath channel is fixed for a one sub-slot duration ( $T_\ell + T_{GI}$ ) in absence of the Doppler effect. It supports the circularity assumption of the multipath channel. Therefore, in the same environmental condition for LICIS and same multipath channel estimation complexity, we can guarantee the circularity assumption of the multipath channel in period of  $T_\ell + T_{GI}$ . It happens where  $M = \rho \Rightarrow T_\ell = \rho \frac{T_p}{\rho}$ . Therefore, based on (4.24), the spectral efficiency is preserved where  $M = \rho$ .

## 4.4 ICI Distortion Expression

In this part, the ICI distortion powers, in conventional LTE numerology and LICIS, are compared analytically. One RB of the conventional LTE numerology with subcarrier-spacing of  $\Delta f_s$  in a frequency dispersive channel is considered. The ICI power, which affects the  $\zeta^{\text{th}}$  subcarrier in the RB, is given in [40] as

$$\mathcal{P}_{\text{ICILTE}}(\zeta) = \frac{(T_\ell f_{d_{\max}} \sigma_d)^2}{2} \sum_{r=1, r \neq \zeta}^K \frac{1}{(r - \zeta)^2}. \quad (4.25)$$

For the ICI power in LICIS model, (4.6) is rewritten as follows

$$\mathbf{X}_\mu^i[n] = \begin{cases} \frac{1}{\sqrt{T_\rho}} \sum_{r=\lfloor \frac{n}{T_\rho} \rfloor T_\rho}^{(\lfloor \frac{n}{T_\rho} \rfloor + 1) T_\rho} a_r e^{j \frac{2\pi}{T_\rho} (r - \lfloor \frac{n}{T_\rho} \rfloor T_\rho) n} & 0 \leq n \leq \mathcal{L} - 1 \\ 0 & \mathcal{L} \leq n \leq T_i - 1 \end{cases}, \quad (4.26)$$

where  $a_r$  denotes the  $r^{\text{th}}$  data symbol in the frequency domain and  $\lfloor \cdot \rfloor$  is a floor

function. Then similar to (4.25) for conventional LTE numerology, the following ICI power affecting the  $\zeta^{\text{th}}$  subcarrier in one RB is obtained for  $\mathbf{X}_\mu^i$  in LICIS:

$$\mathcal{P}_{\text{ICI}_{\text{LICIS}}}(\zeta) = \frac{(T_\rho f_{d_{\max}} \sigma_d)^2}{2} \sum_{r=1, r \neq \zeta}^{\frac{K}{\rho}} \frac{1}{(r - \zeta)^2}. \quad (4.27)$$

The ICI power in (4.27) is affected by less number of subcarriers ( $\frac{K}{\rho}$ ) along with the smaller multiplier ( $T_\rho$ ) compared to the ICI power in (4.25) for LTE numerology with  $K$  subcarriers and multiplier  $T_\ell$ . Therefore, the less ICI power affects the subcarriers in LICIS and consequently better reliability is expected to be obtained.

## 4.5 Numerical Results

In the simulations, we compare our proposed numerology design with the conventional LTE numerology. Comparisons include: a) symbol error rate (SER) performance in high speed UAV communications, b) spectral efficiency performance, c) average error vector magnitude (EVM) distribution over the subcarriers, and finally d) ICI power versus normalized Doppler shift.

In all of the simulations with sample duration of  $t_s = 0.52 \mu\text{s}$ , the following parameters are considered:  $\Delta f_s = 15 \text{ kHz}$ ,  $M = \rho$ ,  $\mathcal{L} = 128$ ,  $K = 12$ ,  $N_{RB} = 6$ ,  $T_{GI} = 16t_s \mu\text{s}$ , and  $\tau_{max} = 16t_s \mu\text{s}$ . The multipath Rayleigh fading channel is simulated as exponentially decaying power delay profile (PDP) like in Fig. 4.10 with  $\tau_{rms} = 10t_s \mu\text{s}$ . The CFO of the system is set as  $f_\delta = 200 \text{ Hz}$ . The radio frequency transmission band is considered at 1 GHz.

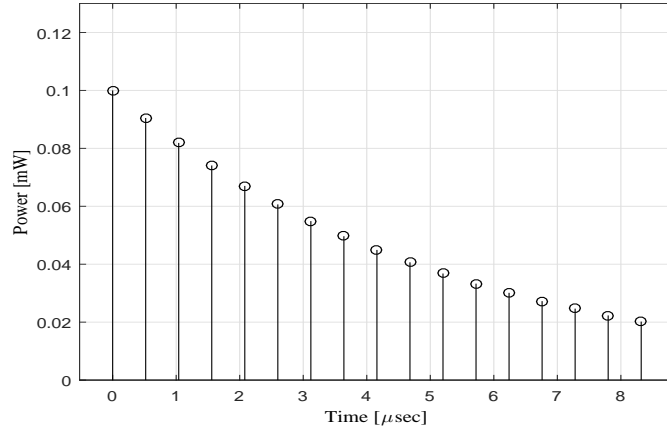


Fig. 4.10: PDP of the multipath Rayleigh fading channel without Doppler effect ( $\tau_{\max} = 16t_s$ ).

### 4.5.1 Symbol Error Rate Performance

In order to show the SER performance of the LICIS in a high speed UAV communications scenario, two different user speeds are considered as 200 km/h and 500 km/h. The maximum Doppler shift equals 1050 Hz and 2850 Hz, respectively. The Doppler shift for each subcarrier is a fraction of reference subcarrier-spacing ( $\Delta f_s = 15$  kHz). The ratio of frequency shift over subcarrier-spacing is defined as the normalized Doppler shift.

Fig. 4.11 depicts the SER performance of LICIS for different subcarrier-spacings compared to the conventional LTE numerology where the user speed is 200 km/h. By going toward the higher speed communications, the better understanding of SER performance improvement of the LICIS can be concluded as shown in Fig. 4.12. LICIS with the subcarrier-spacing of  $\Delta f_p = 120$  kHz gains a remarkable performance improvement compared to the conventional LTE numerology with ZF equalizer. Indeed, this is obtained by utilizing 8 times larger subcarrier-spacing than the reference subcarrier-spacing.

### 4.5.2 Spectral Efficiency Evaluation

Fig. 4.13 compares the spectral efficiency of the LICIS and conventional LTE numerology in the high speed UAV communications where the user speed is

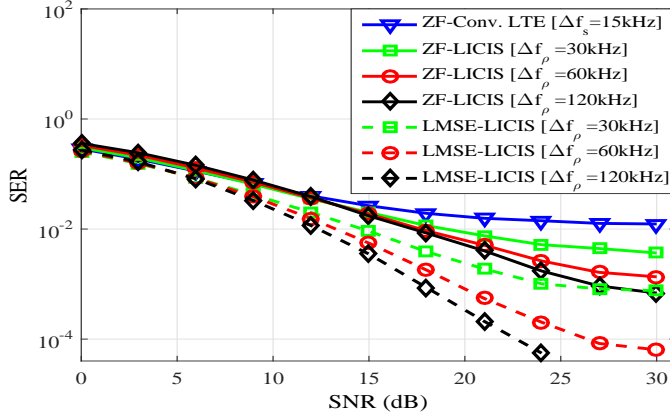


Fig. 4.11: 4-QAM SER performance comparison where  $V_\mu = 200$  km/h and  $f_{d_{\max}} = 0.07\Delta f_s$  ( $M = \rho$ ).

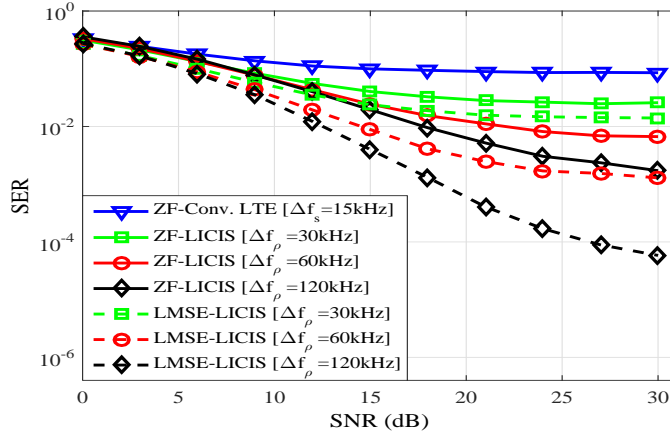


Fig. 4.12: 4-QAM SER performance comparison where  $V_\mu = 500$  km/h and  $f_{d_{\max}} = 0.19\Delta f_s$  ( $M = \rho$ ).

$V_\mu = 500$  km/h. The 4-QAM modulation is used in this simulation and consequently  $\Lambda = 4$ . The LICIS, with  $\Delta f_\rho = 120$  kHz, outperforms the conventional LTE numerology around 10% in high SNRs. The superior improvement of the spectral efficiency in LICIS compared to the conventional LTE numerology is observed in Fig. 4.14 where the higher QAM modulation order such as 64-QAM is used ( $\Lambda = 64$ ). It is worth noting that the conventional LTE numerology with 64-QAM even has worse spectral efficiency performance than 4-QAM in UAV communications with speed of  $V_\mu = 500$  km/h. It happens due to the high sensitivity of conventional LTE symbol boundary alignment numerology to the severe

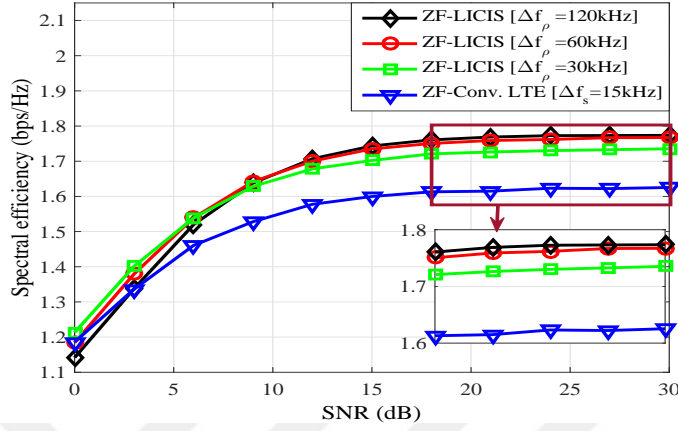


Fig. 4.13: 4-QAM spectral efficiency performance comparison where  $V_\mu = 500$  km/h and  $f_{d_{\max}} = 0.19 \Delta f_s$  ( $M = \rho$ ).

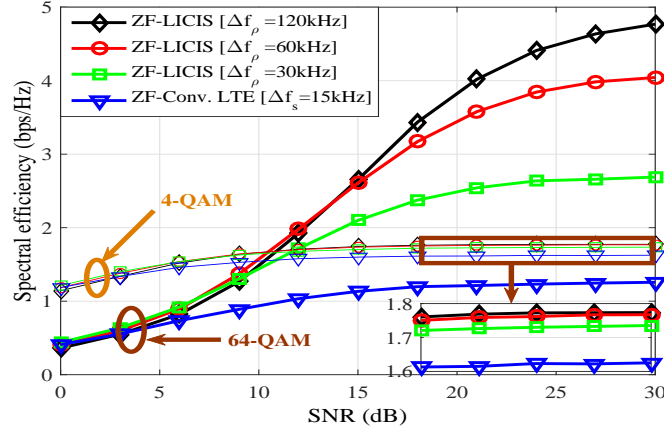


Fig. 4.14: 64-QAM and 4-QAM spectral efficiency performance comparison where  $V_\mu = 500$  km/h and  $f_{d_{\max}} = 0.19 \Delta f_s$  ( $M = \rho$ ).

Doppler shifts.

### 4.5.3 Average Error Vector Magnitude Distribution

In order to see how the subcarriers are located and how ICI problem affects the EVM, the average EVM for each subcarrier is given in Fig. 4.15 where  $V_\mu = 500$  km/h. As shown in this figure, in the conventional LTE numerology, subcarriers have small subcarrier-spacing ( $\Delta f_s = 15$  kHz) but there are more subcarriers in a given BW. By going toward the LICIS and increasing subcarrier-spacing ( $\Delta f_\rho$ ) the number of subcarriers decreases in the BW. As a result, the



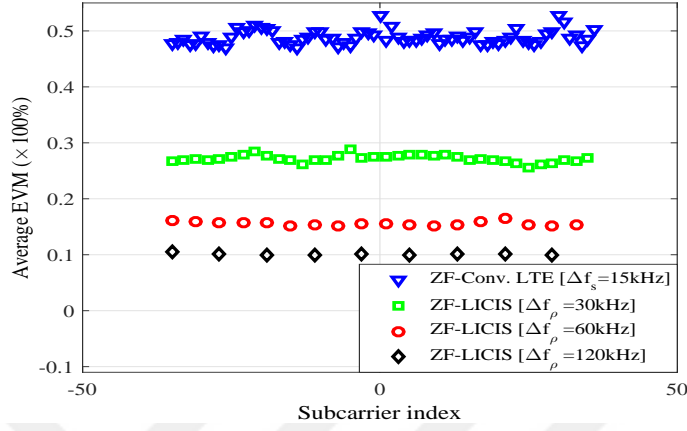


Fig. 4.15: 4-QAM EVM distribution comparison where  $V_\mu = 500$  km/h and  $f_{d_{\max}} = 0.19 \Delta f_s$ .

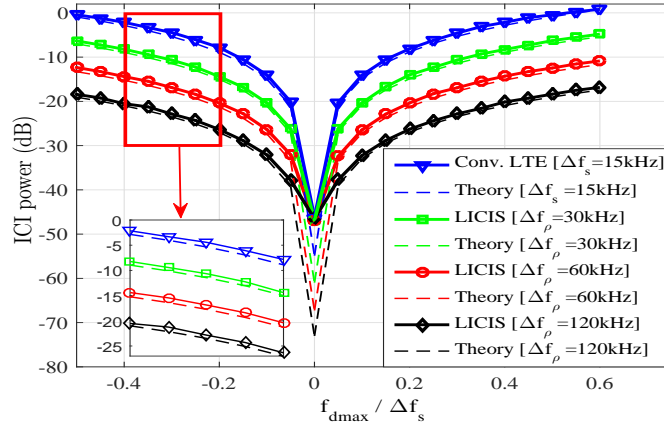


Fig. 4.16: Simulation and theoretical results for the ICI power on a subcarrier versus normalized frequency Doppler shift.

EVM due to the ICI on each subcarrier decreases remarkably. Furthermore, the less subcarriers leads to have less peak to average power ratio which is an advantage in power amplifier selection as well.

#### 4.5.4 ICI power versus normalized Doppler shift

Fig. 4.16 confirms the accuracy of the LICIS analysis where the analytical ICI power for one subcarrier closely agrees with the simulation results. It illustrates the variation of ICI power for one subcarrier versus the normalized Doppler shift.

It is evident that by increasing the normalized Doppler shift, the ICI power increases. However, the increment of the ICI power in LICIS with  $\Delta f_\rho = 120$  kHz is outstandingly (around 18 dB) less than the conventional LTE numerology.

## 4.6 Conclusions

In this work, a novel symbol boundary alignment with respect to OFDM waveform is proposed to reduce the ICI while preserving the spectral efficiency. The analytical forms of the ICI power and spectral efficiency are derived and closely match with the simulation results. e.g., around 18 dB ICI power reduction along with the 10% spectral efficiency enhancement compared to the conventional LTE numerology is achieved with subcarrier-spacing of 120 kHz and 4-QAM modulation in high speed UAV communications. Furthermore, the complexity increment of LICIS is compared to the conventional LTE system and results in an acceptable complexity increment compared to that of already existing solutions. Additionally, it is in compatibility with the current radio access numerologies. Other potential advantage of LICIS is that it utilizes less subcarriers in a given BW compared to the conventional LTE numerology leading to a lower peak to average power ratio and consequently requires less complex power amplifiers as well. In general, the LICIS is a spectral efficient solution with a reasonable complexity increment for the ICI problem in high speed UAV communications.

# Chapter 5

## Concluding Remarks

### 5.1 Summary

In this dissertation, we investigated the design of new waveform design and new symbol boundary alignment to avoid the drawbacks of current waveform and symbol boundary alignment in 5G.

In chapter 2, we proposed an improved version of the ZT DFT-s OFDM which strongly mitigates the ISI problem of ZT DFT-s OFDM. Advantages of the proposed waveform are low PAPR and low OOB emission. Whereas the highlighted ones are its adaptivity in length of ZW and its superior BER performance in time dispersive channels. With the adaptivity that DFT-s ZW OFDM provides, different lengths of ZW can exist within the same resource block while the orthogonality is kept. This adaptivity along with the remarkable performances provided by acceptable complexity causes that DFT-s-ZW-OFDM outperforms other mentioned candidate waveforms.

In chapter 3, we considered a co-existence waveform of ZT DFT-s OFDM and DFT-s ZW OFDM. The proposed model is considered as an hybrid waveform which utilizes the advantages of both waveforms while preventing their disadvantages. The hybrid waveform gives a high flexibility in terms of guard interval, BER performance, power consumption and PAPR without using any extra guard

band or guard interval.

Finally, in chapter 4, we showed that how the current symbol boundary alignments can be changed in order to provide a huge improvement in the performance of the communications. In this part, a new symbol boundary alignment is proposed to reduce the ICI problem while preserving the spectral efficiency. The complexity of this new symbol alignment is acceptable and easily can be compatible with the high and low speed communication systems without creating any problem.



# Bibliography

- [1] “5G Use Cases and Requirements,” White Paper, Nokia Solutions and Networks, 2014.
- [2] H. Lin, “Flexible Configured OFDM for 5G Air Interface,” in *IEEE Access*, vol. 3, no. , pp. 1861-1870, 2015.
- [3] N. Tadayon, G. Kaddoum and R. Noumeir, “Inflight Broadband Connectivity Using Cellular Networks,” in *IEEE Access*, vol. 4, no. , pp. 1595-1606, 2016.
- [4] G. Berardinelli, F. Tavares, T. Sørensen, P. Mogensen and K. Pajukoski, “Zero-tail DFT-spread-OFDM Signals,” in *Globecom Workshops (GC Workshops)*, Atlanta, Georgia, USA, 2013, pp. 229-234.
- [5] G. Berardinelli, F. M. L. Tavares, T. B. Sorensen, P. Mogensen and K. Pajukoski, “On the Potential of Zero-Tail DFT-Spread-OFDM in 5G Networks,” in *IEEE 80th Vehicular Technology Conference (VTC2014-Fall)*, Vancouver, BC, 2014, pp. 1-6.
- [6] F. Schaich and T. Wild , “Waveform Contenders for 5G-OFDM vs. FBMC vs. UPMC,” in *Communications, Control and Signal Processing (ISCCSP)*, Athens, Greece, 2014, pp. 457-460.
- [7] F. Boroujeny, “OFDM Versus Filter Bank Multicarrier,” in *IEEE Signal Processing Magazine*, no. 3, 2011, pp. 92 - 112.

- [8] X. Zhang, M. Jia, L. Chen, J. Ma and J. Qiu, "Filtered-OFDM Enabler for Flexible Waveform in The 5th Generation Cellular Networks," in *IEEE Globecom*, San Diego, CA, USA, 2015, pp. 1-6.
- [9] N. Michailow, M. Matthe, I. Gaspar, A. Caldevilla, L. Mendes, A. Festag and G. Fettweis, "Generalized Frequency Division Multiplexing for 5th Generation Cellular Networks," in *IEEE Transactions on Communications*, vol. 62, no. 9, 2014, pp. 3045-3061.
- [10] A. Onic, "Receiver Concepts for Unique Word OFDM," PhD thesis, Alpen-Adria-University at Klagenfurt, 2013.
- [11] M. Huemer, C. Hofbauer, A. Onic, J. B. Huber, "Design and analysis of UW-OFDM signals," in *AEU - International Journal of Electronics and Communications*, vol. 68, Oct. 2014, pp. 958-968.
- [12] H. Jung, M. Cudak, K. Baum and V. Nangia, "Impact of Out-of-Band Emission in OFDM and in DFT-SOFDM," in *Vehicular Technology Conference (VTC Spring)*, Barcelona, Spain, 2009.
- [13] A. Şahin, R. Yang, M. Ghosh and R. Olesen, "An Improved Unique Word DFT-Spread OFDM Scheme for 5G Systems," in *IEEE Globecom Workshops (GC Wkshps)*, San Diego, CA, USA, 2015, pp. 1-6.
- [14] K. Sankar, "Inter Carrier Interference (ICI) in OFDM due to frequency offset", [Online] Available: <http://www.dsplog.com/2009/08/08/effect-of-ici-in-ofdm/>
- [15] J. Wu and P. Fan, "A Survey on High Mobility Wireless Communications: Challenges, Opportunities and Solutions," in *IEEE Access*, vol. 4, no. , pp. 450-476, 2016.
- [16] C. R. Sheu, J. W. Liu and C. C. Huang, "A Low Complexity ICI Cancellation Scheme with Multi-Step Windowing and Modified SIC for High-Mobility OFDM Systems," in *2010 IEEE 71st Vehicular Technology Conference*, Taipei, Taiwan, 2010, pp. 1-5.

- [17] J. Armstrong, "Analysis of new and existing methods of reducing intercarrier interference due to carrier frequency offset in OFDM," in *IEEE Transactions on Communications*, vol. 47, no. 3, pp. 365-369, Mar 1999.
- [18] K. Y. Lin, H. P. Lin and M. C. Tseng, "An Equivalent Channel Time Variation Mitigation Scheme for ICI Reduction in High-Mobility OFDM Systems," in *IEEE Transactions on Broadcasting*, vol. 58, no. 3, pp. 472-479, Sept. 2012.
- [19] X. Li, R. Zhou, V. Chakravarthy, S. Hong and Z. Wu, "Total Intercarrier Interference Cancellation for OFDM Mobile Communication Systems," in *2010 7th IEEE Consumer Communications and Networking Conference*, Las Vegas, NV, 2010, pp. 1-5.
- [20] Z. Mokhtari and M. Sabbaghian, "Near-Optimal Angle of Transform in FrFT-OFDM Systems Based on ICI Analysis," in *IEEE Transactions on Vehicular Technology*, vol. 65, no. 7, pp. 5777-5783, July 2016.
- [21] K. Kambara, H. Nishimoto, T. Nishimura, T. Ohgane and Y. Ogawa, "Sub-block processing in MMSE-FDE under fast fading environments," in *IEEE Journal on Selected Areas in Communications*, vol. 26, no. 2, pp. 359-365, February 2008.
- [22] V. Vakilian, T. Wild, F. Schaich, S. ten Brink and J. F. Frigon, "Universal-filtered multi-carrier technique for wireless systems beyond LTE," in *2013 IEEE Globecom Workshops (GC Wkshps)*, Atlanta, GA, 2013, pp. 223-228.
- [23] A. R. Jafri, J. Majid, M. A. Shami, M. A. Imran and M. Najam-Ul-Islam, "Hardware Complexity Reduction in Universal Filtered Multicarrier Transmitter Implementation," in *IEEE Access*, vol. 5, no. , pp. 13401-13408, 2017.
- [24] T. Wild, F. Schaich and Y. Chen, "5G air interface design based on Universal Filtered (UF-)OFDM," in *19th International Conference on Digital Signal Processing*, Hong Kong, 2014, pp. 699-704.
- [25] R1-162204, " Numerology requirements", Qualcomm Incorporated, Busan, RAN1#84, Korea, Apr. 11th - 15th, 2016, [Online]. Available:

[http://www.3gpp.org/ftp/TSG\\_RAN/WG1\\_RL1/TSGR1\\_84b/Docs/R1-162204.zip](http://www.3gpp.org/ftp/TSG_RAN/WG1_RL1/TSGR1_84b/Docs/R1-162204.zip)

- [26] R1-166939, “Numerology evaluation results for high speed scenario”, ETRI, RAN1#86, Gothenburg, Sweden, Aug. 22th - 26th, 2016, [Online]. Available:[http://www.3gpp.org/ftp/tsg\\_ran/WG1\\_RL1/TSGR1\\_86/Docs/R1-166939.zip](http://www.3gpp.org/ftp/tsg_ran/WG1_RL1/TSGR1_86/Docs/R1-166939.zip)
- [27] G. Berardinelli, K. I. Pedersen, F. Frederiksen, P. E. Mogensen, “On the design of a Radio Numerology for 5G Wide Area”, in *ICWMC 2015, The Eleventh International Conference on Wireless and Mobile Communications*. IARIA, 2015. p. 13-18.
- [28] B. Muquet, Zhengdao Wang, G. Giannakis, M. de Courville and P. Duhamel, “Cyclic Prefixing or Zero Padding for Wireless Multicarrier Transmissions?,” in *IEEE Transactions on Communications*, vol. 50, no. 12, pp. 2136-2148, Dec 2002.
- [29] G. Berardinelli, K. I. Pedersen, T. B. Sorensen and P. Mogensen, “Generalized DFT-Spread-OFDM as 5G Waveform,” in *IEEE Communications Magazine*, vol. 54, no. 11, pp. 99-105, November 2016.
- [30] Keysight Technologies, Inc. “LTE Physical Layer Overview”, 2017, [Online]. Available: [http://rfmw.em.keysight.com/wireless/helpfiles/89600b/webhelp/subsystems/lte/content/lte\\_overview.htm](http://rfmw.em.keysight.com/wireless/helpfiles/89600b/webhelp/subsystems/lte/content/lte_overview.htm)
- [31] R1-167027, “NR Numerologies”, KT Corp, , RAN1#86, Gothenburg, Sweden, Aug. 22th - 26th, 2016, [Online]. Available: [http://www.3gpp.org/ftp/tsg\\_ran/WG1\\_RL1/TSGR1\\_86/Docs/R1-167027.zip](http://www.3gpp.org/ftp/tsg_ran/WG1_RL1/TSGR1_86/Docs/R1-167027.zip)
- [32] W. Rhee, N. Xu, B. Zhou, and Z. Whang, “Fractional-N Frequency Synthesis Overview and Practical Aspects with FIR-Embedded design”, in *Journal of Semiconductor Technology and Science*, April 2013, pp. 170-183.



- [33] Y. S. Cho, J. Kim, W. Y. Yang, C. Kang, Introduction to OFDM, in *Mimo-OFDM Wireless Communications with MATLAB*, 1st ed. WILEY, 2010, ch. 4, sec. 2, pp. 128135
- [34] B. Muquet, Zhengdao Wang, G. B. Giannakis, M. de Courville and P. Duhamel, "Cyclic prefixing or zero padding for wireless multicarrier transmissions?," in *IEEE Transactions on Communications*, vol. 50, no. 12, pp. 2136-2148, Dec 2002.
- [35] A. Scaglione, G. B. Giannakis and S. Barbarossa, "Redundant filterbank precoders and equalizers. II. Blind channel estimation, synchronization, and direct equalization," in *IEEE Transactions on Signal Processing*, vol. 47, no. 7, pp. 2007-2022, Jul 1999.
- [36] J. H. Manton and Yingbo Hua, "A frequency domain deterministic approach to channel identification," in *IEEE Signal Processing Letters*, vol. 6, no. 12, pp. 323-326, Dec. 1999.
- [37] S. Ahmed and H. Arslan, "Evaluation of frequency offset and Doppler effect in terrestrial RF and in underwater acoustic OFDM systems," in *MILCOM 2008 - 2008 IEEE Military Communications Conference*, San Diego, CA, 2008, pp. 1-7.
- [38] G. Wunder, et.al., 5GNOW: Non-Orthogonal Asynchronous Waveforms for Future Mobile Applications, in *IEEE Communications Magazine*, February 2014, pp.97-10
- [39] B. Farhang-Boroujeny, "OFDM Versus Filter Bank Multicarrier," in *IEEE Signal Processing Magazine*, vol. 28, no. 3, pp. 92-112, May 2011.
- [40] T. R. Wang, J. G. Proakis, E. Masry, and J. Zeidler, "Performance Degradation of OFDM Systems Due to Doppler Spreading," in *IEEE Trans. Wireless Commun.*, vol. 5, no. 6, pp. 14221432, June 2006.

# ON THE DESIGN OF A FLEXIBLE WAVEFORM AND LOW ICI SYMBOL BOUNDARY ALIGNMENT

## ORIGINALITY REPORT

10%

SIMILARITY INDEX

7%

INTERNET SOURCES

8%

PUBLICATIONS

1%

STUDENT PAPERS

## PRIMARY SOURCES

- 1** Berardinelli, Gilberto, Fernando M. L. Tavares, Troels B. Sorensen, Preben Mogensen, and Kari Pajukoski. "On the Potential of Zero-Tail DFT-Spread-OFDM in 5G Networks", 2014 IEEE 80th Vehicular Technology Conference (VTC2014-Fall), 2014.

Publication

1%
- 2** Alphan Sahin, Rui Yang, Erdem Bala, Mihaela C. Beluri, Robert L. Olesen. "Flexible DFT-S-OFDM: Solutions and Challenges", IEEE Communications Magazine, 2016

Publication

1%
- 3** [alphan.myweb.usf.edu](http://alphan.myweb.usf.edu)

Internet Source

1%
- 4** [thinkmind.org](http://thinkmind.org)

Internet Source

<1%
- 5** Submitted to Higher Education Commission Pakistan

Student Paper

<1%